ABSTRACT

Title of Document: DEVELOPMENT OF FATIGUE MODELS FOR COPPER TRACES ON PRINTED WIRING ASSEMBLIES UNDER QUASI-STATIC CYCLIC MECHANICAL BENDING.

Daniel M Farley, Doctor of Philosophy, 2010

Directed By: Professor Abhijit Dasgupta
Department of Mechanical Engineering

This dissertation investigates the fatigue durability of copper (Cu) traces on printed wiring assemblies (PWAs) under quasi-static cyclic mechanical flexure, using experimental results from a set of three-point bending fatigue tests, finite element (FE) modeling of the stresses generated during the cyclic bending tests, and response surfaces (RS) to facilitate iterative assessment of the model constants.

Cyclic three-point bend tests were conducted on land grid array (LGA) components during this investigation. Failure analysis revealed the fatigue failure sites to be in the Cu traces, at the outer edge of the foot-print of the solder joint. A three-dimensional, elastic-plastic FE model simulating the event (based on a global and local modeling strategy) was used to determine the stresses and strains occurring at the failure site during the cyclic loading. Parametric studies were conducted to examine the influence of elastic-plastic constitutive behavior on the stress and strain

states at the failure site. Results of the parametric studies were captured in compact meta-models, using polynomial response surfaces. The durability data was collected from the experiment and used in conjunction with these models, to develop a set of compatible constitutive and fatigue model constants that best fit the behavior observed.

Since the loading was not fully reversed, a mean stress correction factor was needed. Existing correction methods, such as the modified Morrow model, were found to be deficient for tensile means stresses, due to high mean stresses predicted by classical constitutive models. A new correction model was proposed, based on a "tanh" term, which forced a saturation of the mean stress effect at higher stress levels for tensile means stresses. This saturation effect was also considered for compressive loading, termed the BCS model ("B" for "bounded" effect of the mean stresses), and compared with the standard unbounded model, termed the UCS model.

A detailed iterative methodology was developed to iterate the Cu elastic-plastic constitutive model constants as well as the cyclic fatigue model constants needed to satisfy the observed durability behavior. This iterative model was based on the average strain values in cross section of the trace, at the failure site. The resulting fatigue model constants were termed the "averaged fatigue constants (AFCs).

To further improve on the fatigue constants, the fatigue damage initiation and propagation behavior were considered separately, using a continuum damage mechanics method termed the successive initiation method. In this phase of the

study, the constitutive model constants were those determined from the AFC model. This method uses an incremental damage growth concept rather than a classical fracture propagation concept, since there is distributed damage observed in the experiment. The resulting fatigue constants were termed the incremental fatigue constants (IFCs).

Finally, the validity of the modeling approach and the developed AFC and IFC model constants are explored, using results from a published case study of four-point cyclic bend tests of leadless chip resistors (LCRs). The model appears to predict the results reasonably well.

DEVELOPMENT OF FATIGUE MODELS FOR COPPER TRACES ON PRINTED WIRING ASSEMBLIES UNDER QUASI-STATIC CYCLIC MECHANICAL BENDING.

By

Daniel M Farley

Dissertation submitted to the Faculty of the Graduate School of the
University of Maryland, College Park, in partial fulfillment
of the requirements for the degree of
Doctor of Philosophy
2010

Advisory Committee:
Professor Abhijit Dasgupta, Chair/Advisor
Professor Bongtae Han
Professor Peter Sandborn
Associate Professor F. Patrick McCluskey
Professor Charles Schwartz, Dean's Representative

Dedication

Dedicated to my lovely and beautiful *neamhspleach*, Ms. Molly Quell. I couldn't have done this… or, hell, anything… without you.

I love you.

Acknowledgements

If left unchecked, this section could go on like an Oscars acceptance speech being slowly drowned out by the orchestra. So I'll be brief.

I could not have gotten to this point without the help of so many people. Like Joe Varghese, taking me under his slightly more experienced wing when I got to Maryland. The guys at Philips that I've worked with throughout my time here, regardless of how many times they changed their research interests, Jo Caers and Hans De Vries. All my friends and classmates that helped ease the stress on the weekends and, yes, sometimes weeknights, when we needed it. My labmates Gayatri Cuddalorepatta, Shaughn London, Yuxun Zhou, Stuart Douglas, and Koustav Sinha. And of course, Dr. Moustafa Al-Bassyiouni. The German exchange students I've worked with over the years, starting with Mike Michaeli. You always remember "your first German". My mother, Kathleen Desrosiers, who played an early role by not letting me take a break from undergrad to work a "real job" and finally make some money. My sister, Shannon Farley and the awesome little niece and nephew she and her husband Jay Durand have given me. And yeah, even all the residents of Bloomingdale, DC that I've met over the years and come to love. Also, the Quell Clan: Molly's parents, Garry and Jenny; and brother Luke. I'll even include the Murphy dog, and all that unconditional love he still gives me on days I don't feel like I deserve it.

But most of all, aside from the one to whom this is dedicated: my love Ms. Molly Quell… most of all thanks go to my advisor, *The Boss*, Abhijit Dasgupta. A-dawg. Captain of the A-Team. We had our ups and downs, ins and outs, but he stuck with me. And now I'm Dr. Dan.

Table of Contents

List of Tables

List of Figures

Chapter 1: Introduction to Thesis

1.1 Problem Statement

With the consumer electronics industry constantly seeking out new ways to decrease the size of its products, many methods of miniaturization of electronic circuits are being explored [1-5]. With new methods, architectures, and structures come new reliability concerns. While reliability and failure studies generally focus on the solder joints of electronics, an increase in other failure sites is being noticed. This study focuses on the occurrence of copper (Cu) trace cracks just outside the solder joint, and offers up a new formation of fatigue model with model constants for the assessment of the Cu.

1.2 Motivation & Background

This investigation, in fact, started out as an assessment of the solder interconnects on a new land-grid array (LGA) package, undergoing mechanical shock and cycling. The solder joints for this LGA, as in many LGAs, are short and squat, tending toward a more robust behavior in mechanical loading. Sure enough, failure analysis of the solder joints revealed no solder failures.

Going forward with the assessment and using standard fatigue models for the SAC solder used in the LGA, the fatigue model in fact over-predicted the lifetime of the components in both the drop and bend tests.

Moving on to new and different failure analysis techniques such as Dye & Pry and Lateral Polishing finally revealed the source of the component failures: Cu trace

cracks just outside the edge of the solder joints. It was theorized that the solder edge created a stress concentration area that led to the competing failure mechanism of Cu fatigue to win out. It was then decided that the Cu fatigue should be investigated.

1.3 Literature Review

The following subsections give a brief description of the topic and identify which sections of the following chapters will discuss the literature on that topic.

1.3.1 Copper Fatigue in Microelectronics

Copper (Cu) fatigue in microelectronics is a sometimes overlooked topic of discussion, since many studies tend to head right for the solder issues. Especially with all of the progress made and as of yet undiscovered details about the new Pb-free solder alloys, Cu trace fatigue doesn't get much attention. This topic will be discussed in Chapters 2, 3, and 4.

1.3.2 Response Surface Modeling Methods

The Response Surface (RS) is a concept wherein many inter-related variables can be tied together mathematically. It is a time and computation saving device, in this study, and will be discussed in Chapter 2.

1.3.3 Mean-stress Effects in Cyclic Fatigue

The mean stress effects in cyclic fatigue are borne of a not fully reversed loading profile, giving a nonzero average cyclic stress. This concept is essential to this study and will be discussed in Chapters 2 and 3.

1.4 Overview of thesis document

Chapter 2 describes the development of the fatigue model using constants based on the average cross section of the Cu trace (AFCs). Along the way to this development, the finite element (FE) models used and response surfaces (RS) formulated that are used in conjunction with the experimental work of 3-point (3PT) cyclic bend tests are described.

Chapter 3 shows the extension of the AFC work to a more precise crack treatment. This section describes the development of the fatigue model and constants based on incremental fatigue assessments (IFCs). Here, successive initiation (SI) is used to model discrete amounts of the Cu trace failure site cross section initiating a crack, and then a new crack next to that, and so on across the whole trace until total failure.

Chapter 4 takes the fatigue model and constants of both the AFCs and the IFCs and applies them to 4-pont (4PT) cyclic bend test results on 2512 SMT resistors on a PWB. The resistors have similarly structured solder and Cu trace neck zones to the 3PT specimens.

Chapter 5 serves as the summary. Conclusions and discussions are made, as well as the contributions to the field this dissertation provides. Finally, the limitations of this study are explained, and possible avenues of future work are offered.

Chapter 2: Fatigue Model based on Average Cross-Section Strain

This study focuses on quasi-static mechanical cycling durability of copper traces on printed wiring assemblies (PWAs). PWA specimens populated with Land Grid Array (LGA) components on copper-defined pads were cycled to failure under zero-to-max, three-point bending. Failure is defined in terms of electrical opens due to fatigue damage propagation through the entire cross-section of the trace. Failure statistics were collected and failure analysis was conducted to identify fatigue failures in the copper traces, near the connection to the solder pad.

Cyclic bending of this assembly was modeled with 3D, elastic-plastic, finite deformation (geometrically nonlinear) finite element analysis. Due to the complexity of the geometry, a two-step global-local approach was used to identify the cyclic strain history and the mean-stress at the copper trace failure site.

A generalized strain-based fatigue model is proposed, to characterize the fatigue durability in terms of the amplitude of cyclic strain and the cyclic mean of the hydrostatic stress. The strain and stress values are averaged over the entire cross-section, to be consistent with the failure criterion defined above. Average cross-sectional model constants are iteratively estimated by ensuring that they are simultaneously compatible with both the durability test data and the copper stress-strain curves used in the FEA (finite element analysis). To minimize the computational burden, a Response Surface (RS) [1] was created for the actual

iteration. The key RS variables and their functional inter-relationships were determined from a fractional factorial FEA parametric study.

The important impact of this study includes insight into copper trace failure in PWAs under mechanical cycling, a quantitative model to predict its occurrence, and validated guidelines to prevent it by design.

2.1 Introduction

With the consumer electronics industry constantly seeking out new ways to decrease the size of its products, many methods of miniaturization of electronic circuits are being explored [2-6]. New reliability concerns are an intrinsic part of new methods, architectures and structures. While many PWA reliability and failure studies generally focus on the solder interconnects, an increase in other failure sites is being noticed. This study focuses on the occurrence of copper (Cu) trace damage sites just outside the solder joint, and offers up a new set of fatigue models with model constants, for durability assessment of the Cu traces.

The Background and Motivation as well as a Literature Review are presented in the remainder of this introductory section. Durability tests and test results are described in Section 2.2. In Section 2.3, stresses and strains at the failure site are estimated with finite element simulations of the experimental setup and loading, since the Cu trace is too small for *insitu* experimental measurements. Section 2.4 then describes the development of the fatigue model that describes the observed Cu trace failures.

Summary and conclusions from this work are presented last, along with recommendations for future work.

2.1.1 Background & Motivation

3D multitechnology, multi-functional, multichip packaging technology, usually referred to as a "SiP" (system-in-package), has emerged as one of the leading methods of miniaturization. These packages can be found anywhere miniaturization is needed, from portable electronics, to smart biomechanical implants, Micro-Opto-Electromechanical Systems (MOEMS), biochemical 'lab-on-a-chip' sensors, and even home appliance electronic controls [7, 8]. Additionally, these packages frequently forego leads and even solder balls for further miniaturization. This generally results in stiffer, more robust solder interconnects. Consequently, the mechanically weakest point in the chain becomes the traces on the PWA [9-14].

When assessing the mechanical durability of electronic assemblies, the dominant failure site is generally believed to be in the solder interconnect [13]. However, in many package styles, such as BGAs (ball grid arrays), LGAs (land grid arrays), MLFs (micro lead frame) and QFNs (quad flat no-lead), the Cu trace emanating from the solder pad may be the weakest failure site, especially if the solder joint is copper-defined rather than mask-defined, and if there is a sudden neck in the copper trace with sharp re-entrant corners where the copper trace emanates from the solder pad [12, 14, 15]. This is particularly true in situations with cyclic mechanical loading, such as cyclic quasi-static bending, vibration and repetitive drop/shock [6, 9, 10, 12-14, 16, 17].

2.1.2 Literature Review

This paper investigates the cyclic stress and strain histories in the Cu traces and attempts to quantify the accumulated fatigue damage in terms of these parameters. Prior research by the author had focused on the solder interconnects for this package style [18, 19]. In the present study the focus is on the Cu traces.

The literature reveals many examples where the Cu trace is the weakest point in the system and the dominant failure site [11, 12]. Additionally, these failures have been found to be easily preventable by revision to the trace design. Studies show that redesigned Cu traces can indeed survive repetitive mechanical loading and that the failure site shifts elsewhere [11, 13, 20, 21].

Quantitative insights are needed into the fatigue durability of copper traces so that failures can be predicted and design guidelines can be developed to prevent these failures. The existing literature does not have a consensus of Cu properties for electronics devices [22-25]. It is generally accepted that the Ramberg-Osgood elastic-plastic constitutive model [26] is the best representation of Cu stress-strain response:

$$\epsilon = \frac{\sigma}{E} + \left(\frac{\sigma}{K}\right)^{\frac{1}{n}} \tag{2-1}$$

where ϵ is the equivalent strain, σ is the von Mises' stress, E is the elastic modulus, K is the plastic hardening coefficient, and n is the plastic hardening exponent.

There is a wealth of knowledge already in the literature on copper fatigue, failure, and cracking. A vast amount focuses on grain effects, whether they be size effects or boundary interactions, and how the differences affect fatigue life [27-32]. The Hall-Petch relationship tells us that the strength of a material has a dependence on grain size:

$$\sigma_y = \sigma_0 + k \cdot D^{-1/2} \tag{2-2}$$

where D is the grain size, σ_y is the yield strength, and σ_0 is a material constant. Some Cu is processed ahead of time using equal channel angular pressing (ECAP) [33-35]. This was previously believed to increase fatigue life since it increases plasticity and strength. However, as the processing certainly increases strength, it also increases localized brittleness and microstructural instabilities and Mughrabi and Hoeppel show that these effects essentially cancel each other out [24]. It is based on this observation that this paper does not include grain size effects on the fatigue life.

The majority of papers take a LEFM (linear elastic fracture mechanics) approach to describing the fatigue failure evolution process [29, 30, 36]. This approach is well suited to damage evolution due to growth of a single dominant crack. The fatigue damage observed in the Cu traces in this study, however, appears to develop more in a distributed, meandering intergranular fashion. This headed the investigation away from a FM (fracture mechanics) approach, and more toward a CDM (continuum damage mechanics) approach. Mattila [37] and Syed [13] have offered similar studies, but with less depth, and using existing fatigue models.

Hong and Weil [38] performed a study investigating the fatigue properties of copper foils electrodeposited on chromium mirrors to the dimensions typically found in printed circuits. These experiments were uniaxial tensile tests. In this study, Hong attempts to extract fatigue properties for the copper, based on experimental observations. First and foremost, they begin by determining the constitutive properties for the copper. They conducted stress-controlled, zero-to-max cyclic tests. Hong uses a couple of methods to calculate the low-cycle fatigue exponent 'b' based on the Basquin relation in Equation (2-3) and a form of the Morrow relation Equation (2-4).

$$\Delta\sigma_a = \sigma'_f \left(N_f\right)^b \tag{2-3}$$

$$b = {}^{n}/_{(1+5n)} \tag{2-4}$$

Unfortunately, there appears to be some error in the data reported by Hong, in that the tabulated values of exponents 'n' and 'b' presented in their paper do not satisfy Equation (2-6), from which they were reportedly calculated. Furthermore they are unclear as to whether max stress or cyclic stress range was used in the calculation of fatigue properties. Regardless, he does also present a comparison of monotonic and cyclic constitutive curves. While Hong's is an excellent study, it is not sufficient for the goals of this investigation. Hong only uses uniaxial loading. This does not then account for any shear effects that a von Mises stress, as an octahedral stress, can include. Similarly, Hong does not focus at all on the local strain fields at the failure site. It's not necessary for a simplistic uniaxial loading situation. Further focus is on

the mechanisms of the fatigue failures like dislocations, etc. He does also appear to have applied LEFM.

Later, a parametric study will be discussed in which three different material models for Cu and three different n values (see Equation (2-1)) were explored. In the end, the hardening exponent, n, was held constant in this study. Engelmaier [22] and Hong [38] show that the sensitivity to the cyclic changes in n is very small compared to that of K. Also held constant is the elastic modulus, E, for the same reason. Figure 2-1 shows a constitutive schematic, pointing out the various aspects of a material model and the differences between monotonic and cyclic values. The decision was made to use Engelmaier's E_{Cu} and n_{Cu}. Engelmaier's work using E = 82.7GPa [22, 23] has been used most, and falls in the middle of the field as far as the literature goes.

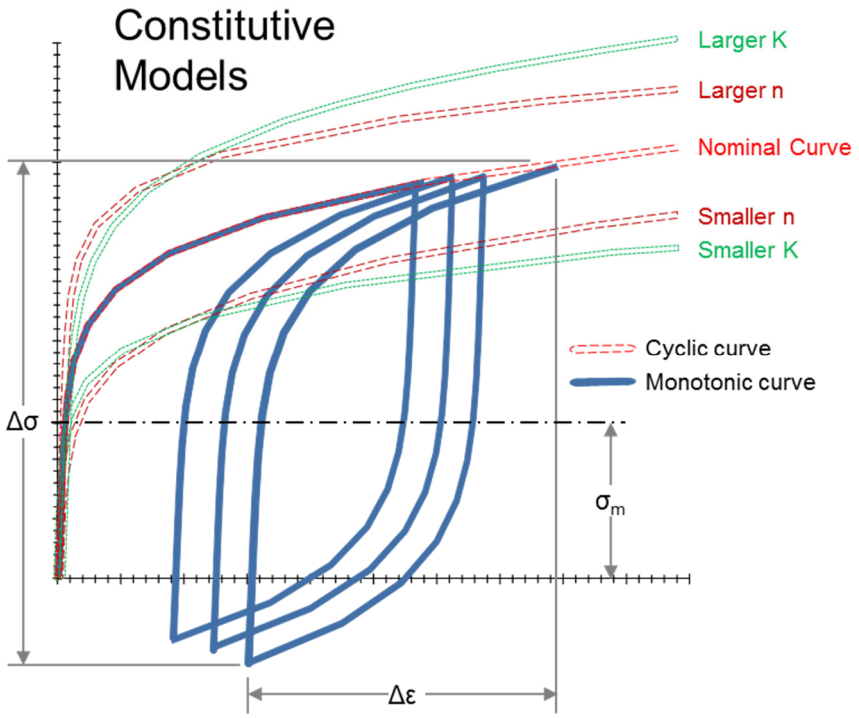

Figure 2-1: General stress-strain schematic showing the hysteresis loops of the monotonic model along with the single (dotted) line of the cyclic model, as well as the effects of varying n and K.

Engelmaier's work [22] has also showed that as the cycles to failure approach 1 or, in other words, as the load tends toward the cyclic fatigue stress, σ'_f, the corresponding monotonic values to σ'_f and the fatigue ductility, ε'_f are lower than expected. Figure 2-2 shows the fatigue curves tending toward a saturation value before $N_f = 1$.

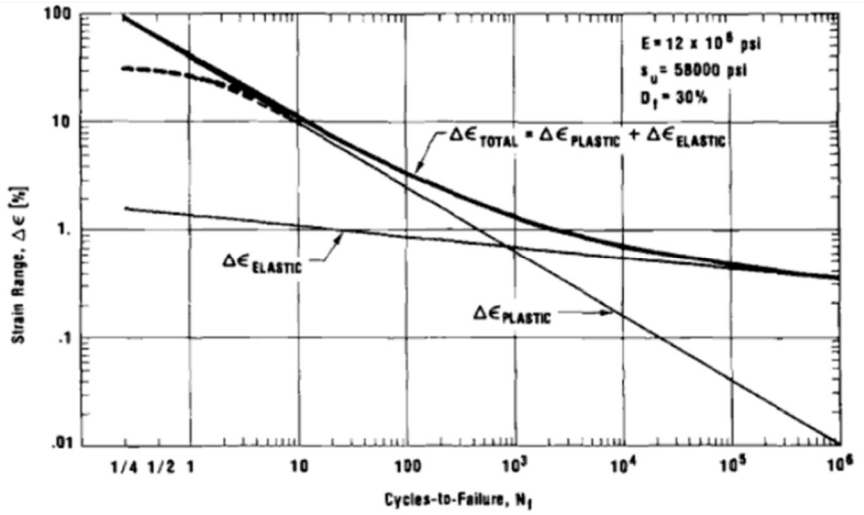

Figure 2-2: [22] Engelmaier's Coffin-Manson plot showing contributions of strains and deviations at extremely low cycles.

As mentioned previously, the relationship between the cyclic and monotonic values in the constitutive models of Cu is shown in Figure 2-1. Engelmaier's transfer functions between cyclic (with apostrophe) and monotonic (without apostrophe) relationships for strength and ductility are Equations (2-5) and (2-6), respectively, which account for the dotted line in Figure 2-2. The cyclic fatigue constants pair of σ'_f and ε'_f, must of course lie on the constitutive curve for Cu. Therefore there is a corresponding cyclic K (K') for the Ramberg-Osgood model in Equation (2-1), when σ'_f and ε'_f, are substituted for σ and ε.

$$\sigma_f = \sigma'_f \left(2N_f\right)^b \quad N_f = {}^1/_4 \tag{2-5}$$

$$\varepsilon_f = \varepsilon'_f \left(2N_f\right)^c \quad N_f = 1½ \tag{2-6}$$

There are many existing fatigue models that are applied to copper fatigue. Most prominent is Sines' model [39], whose general form is seen in Equation (2-7). Sines' model, however, assumes that fatigue durability has a linear dependence on the cyclic mean stress, which does not fit well with the observed behavior in this study. Also well known in the Morrow model, a form of the Sines model, seen in Equation (2-8) [40]. This model proposes a more realistic dependence of durability on the cyclic mean stress, however it can clearly be seen that if the σ_m value surpasses the σ'_f value, the model mathematically falls apart. This may seem physically incorrect, however with the construct of the actual von Mises' yield surface, seen in Figure 2-3, it can be seen that if the principal plan is constantly changing with the stress state, a configuration can occur in which the cyclic mean of the hydrostatic stress (along the hydrostatic axis) could have a magnitude which is greater than the cyclic strength (calculated equivalent stress (or von Mises') stress at the failure surface).

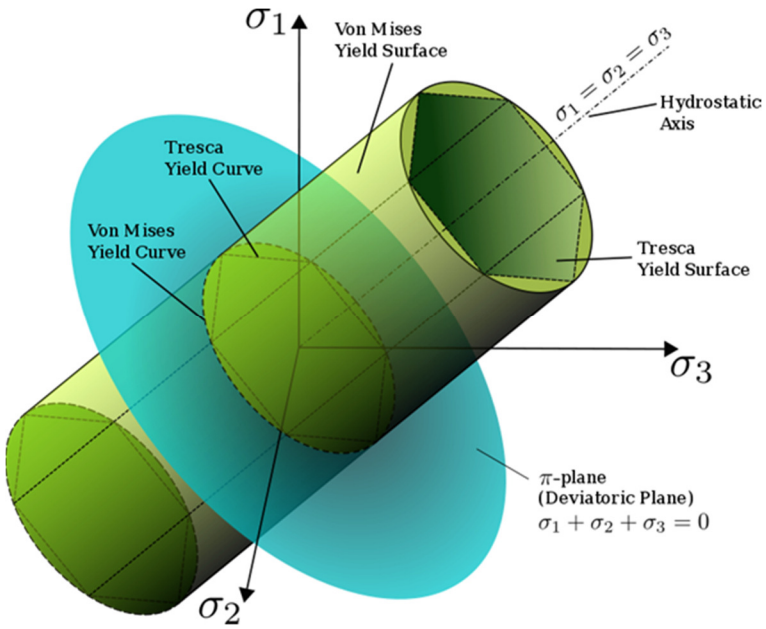

Figure 2-3: Mathematical construct of the von Mises' yield criterion [41].

Two other widely used models are the Smith-Watson-Topper (SWT) model [42], in Equation (2-9) and the Walker model [43], in Equation (2-10). Neither of these allow for empirical correction. Clearly a new model was needed.

$$C - k\sigma_H = \sigma_f (N_f)^b \tag{2-7}$$

$$\frac{\sigma_a}{1 - \frac{\sigma_m}{\sigma_f}} = \sigma_f (N_f)^b \tag{2-8}$$

$$\sqrt{\sigma_{max}\sigma_a} = \sigma_f (N_f)^b \tag{2-9}$$

$$\frac{\sigma_a}{(1-R)^{(W-1)}} = \sigma_f (N_f)^b \tag{2-10}$$

2.2 Experimentation: 3-point Bend Tests

The copper trace fatigue durability data for this study is taken from experimental work presented elsewhere in the literature by the author [20]. This was work done

in conjunction with the author of this study, but performed by co-authors Zhou and De Vries [20]. The test methodology and fatigue results are summarized here for completeness.

2.2.1 Specimen & Test Methodology

The package of interest in this study, shown schematically in Figure 2-4, is an RF SIP component for use in portable electronic products. It contains multiple wirebonded dice, flip-chip dice, and ceramic SMD passives, all on a common substrate. The wirebonded dice are attached to the laminate board with die attach. There are no die stacks in this SiP. The package is fairly stiff because of the many components molded together on a multi-layer substrate and has an LGA architecture, which includes interconnection pads along the perimeter, and a large thermal land in the center.

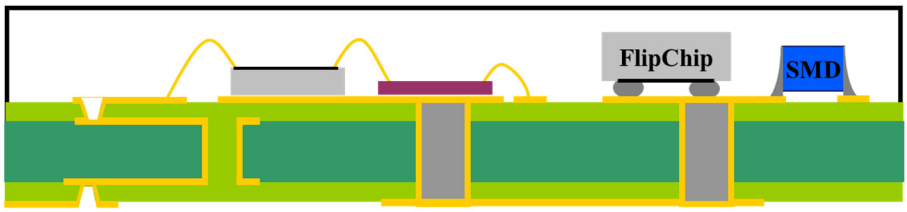

Figure 2-4: SiP schematic

A representation of the PWA specimen used in this study can be seen in Figure 2-6, shown in a standard 3-point flexure setup. These are single-sided PWAs with daisy-chained LGA components grouped into 4 columns of 3 components each, with adequate space between columns to accommodate the center roller without causing any damage. These PWAs are JEDEC (Joint Electron Devices Engineering Council) standard bend test boards. The overall board thickness is 1.56mm, which is a 7-layer

layup pattern with 0.035mm thick metallization layers and 0.475mm thick dielectric layers. The Cu traces are 45µm thick and 120µm wide. The major board dimensions can be seen in Figure 2-5: 48mm wide by 130mm long, with a 90mm wide by 40mm long bend test area. Non-functional daisy-chained components are used, with corresponding daisy chains in the PWB, to facilitate electrical failure monitoring.

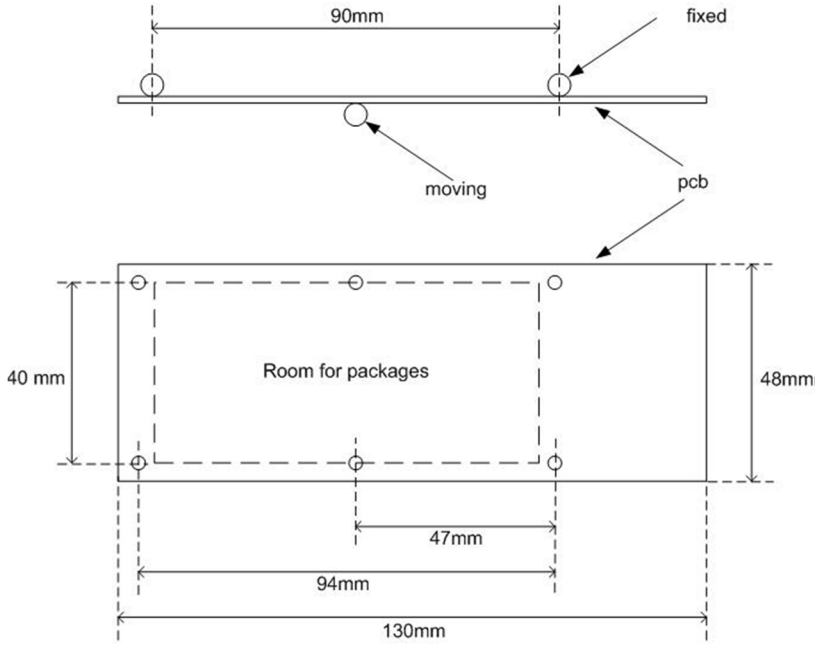

Figure 2-5: Bend test PWA dimensions and roller placement.

The geometry and loading of this specimen are clearly symmetric about the center roller. Three point bending is known to generate a linear gradient of bending moment and curvature along the length of the specimen, as shown schematically in Figure 2-6. Consequently, the stress levels are highest in the interconnects of the inner columns, followed by those of the outer columns. All of the Cu traces emanating from the lands have been angled so as not to be perpendicular to the bend direction, except for those attached to land number one, as shown in Figure 2-7. Although the components are located symmetrically with respect to the center

roller, Land 1 locations are asymmetric since they are located at the top right corner of each component (as shown later in Figure 2-12). Thus the local curvature at Land 1 is different for each column, generating 4 different loading levels in each bend test.

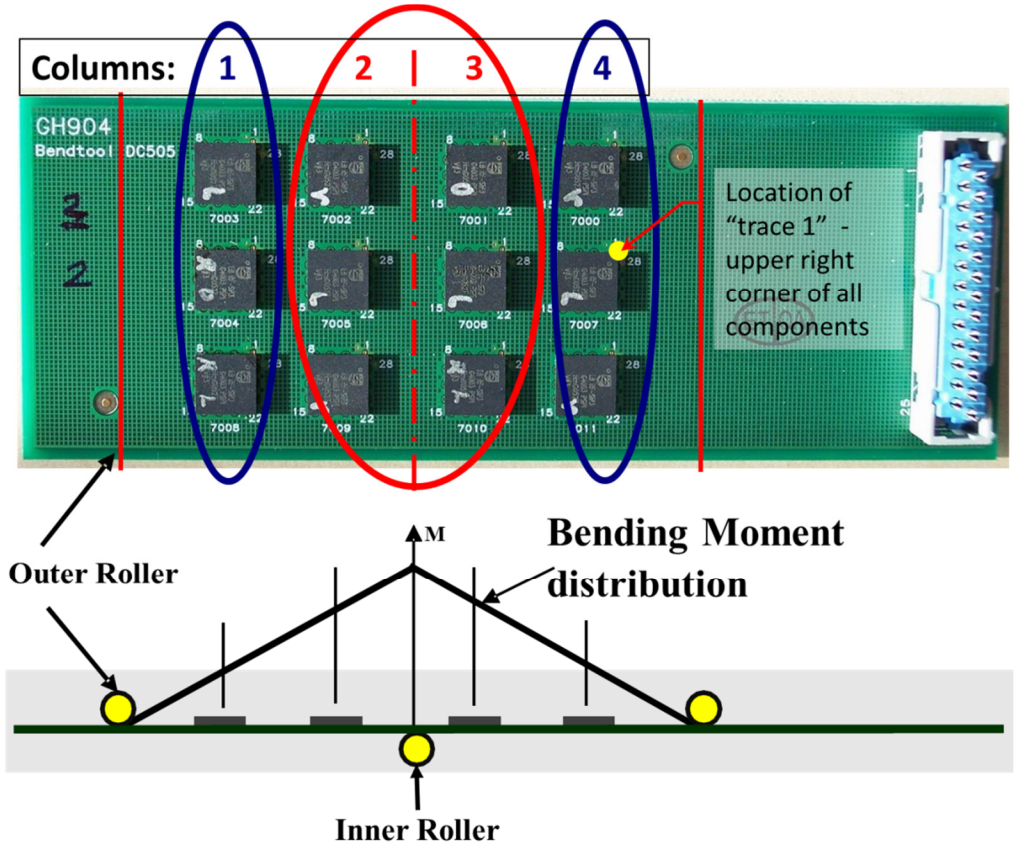

Figure 2-6: '3-point' test board & bending moment diagram. Components within each group (inner & outer rows) are initially expected to experience similar strain distribution.

The test setup and equipment is a custom 3-point bend setup. The board is clamped at the center roller, in an attempt to maintain symmetry. The two outer rollers allow in-plane sliding, to prevent excessive membrane strains in the test specimen. The center roller imposes out-of-plane cyclic movement from zero to max. Since the loading is zero-to-max (R=0) and not completely reversed (R=-1), tests are conducted with PWAs facing both directions in the fixture. Thus, in some tests the

interconnects experience convex curvature (tensile loading) and in some they experience concave curvature (compressive loading).

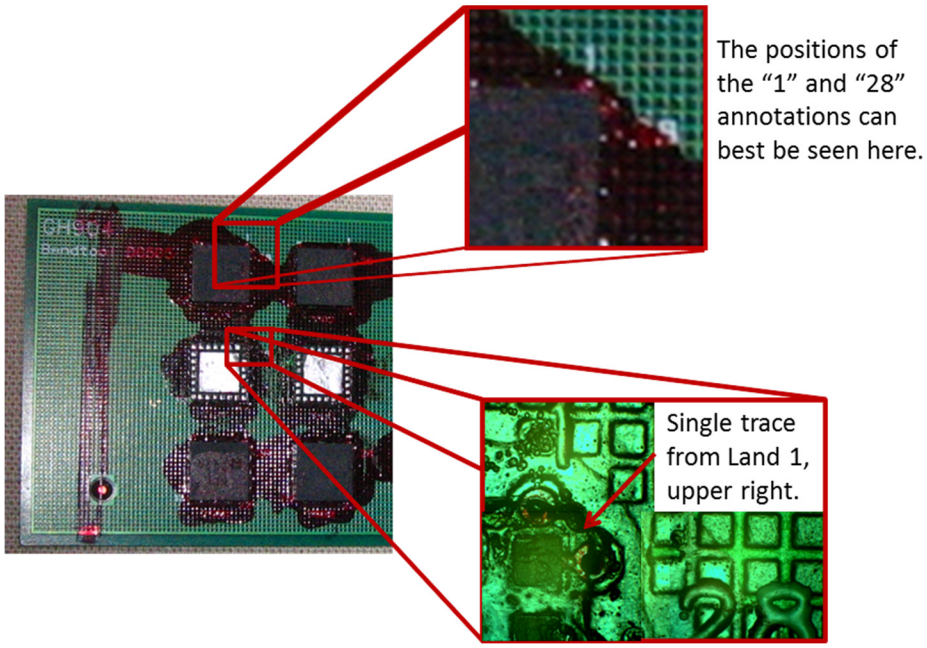

Figure 2-7: An image of a dye-stained test board with insets showing the position of land #1 and the trace attached to it.

The next steps include: (a) overstress tests to determine the destruct limits of the test specimen; (b) failure analysis to determine the dominant failure modes in the overstress tests; (c) selection of AST (accelerated stress test) levels that are below the destruct limits, do not cause failure mechanism shifting, but are sufficiently severe to produce timely failures; and (d) tests and analysis to characterize the specimen response to the entire range of excitations anticipated in the accelerated stress test.

To characterize the specimen for mechanical cycling, a populated test board was subjected to overstress loading, instrumented with strategically placed strain gauges (Figure 2-8) to record the resulting strain levels (Figure 2-10). The overstress tests for

the components showed that a deflection amplitude of about 3mm was sufficient to fail interconnects within the first few mechanical cycles (as shown in Table 2-1). The amplitudes for cyclic testing were therefore kept under 3mm. The overstress tests for the board also showed that the force-deflection curve remained linear within the 3mm deflection envelope (Figure 2-9).

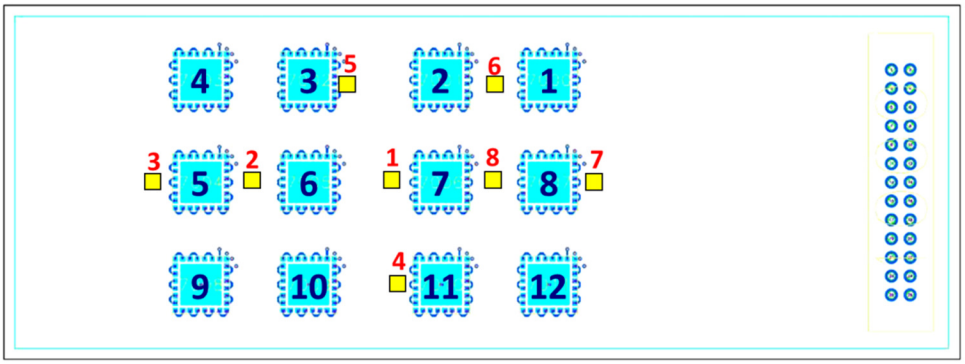

Figure 2-8: Strain gauge locations. The small yellow boxes with the red numbers above them denote the strain gauge locations and their corresponding identifier numbers.

Finally, the board was flexed to each of the load levels meant to be used in the AST, and strain histories were recorded (Figure 2-10).

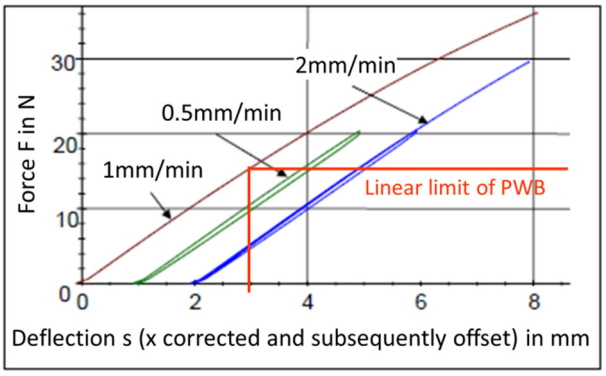

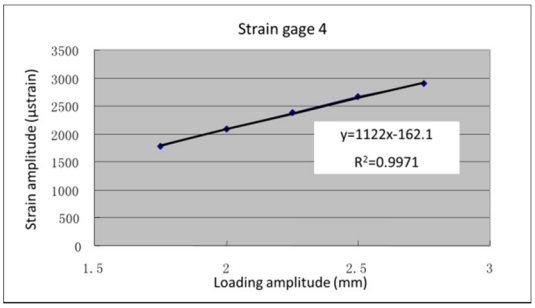

Figure 2-9: PWA Overstress Test Results:
(a) Force-deflection shows the board remains linear within the 3mm deflection envelope, and (b) Strain gauge 4, one of the highest strain regions, shows linearity within the 3mm deflection envelope.

Table 2-1: PWA Overstress Test Results

Overstress Test Result				
Loading Amplitude	2mm	3mm	4mm	5mm
Failed Components	No failure	7 & 11 failed	2 & 3 failed	6 & 10 failed

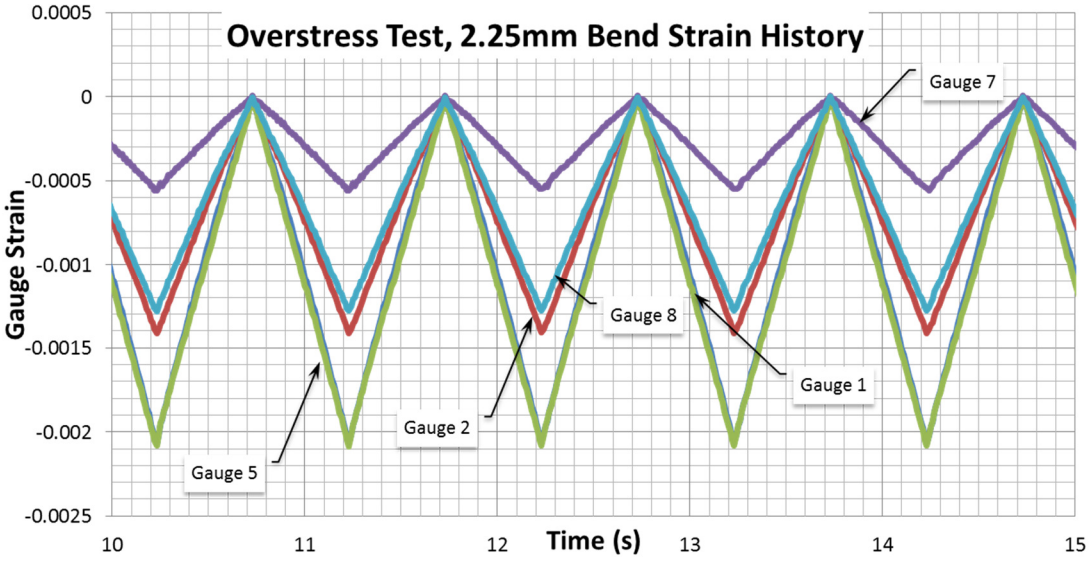

Figure 2-10: Strain levels for selected strain gauges at a selected load level. These data are from a convex 2.25mm amplitude bend. Some asymmetry can be seen between gauges #2 and #8.

Cyclic fatigue testing was performed next. Eight test boards, populated with 12 components each (schematic seen in Figure 2-8), were subjected to 3 different load levels, or "δ values" shown in Table 2-1, to generate sufficient data points on the S-N curve. The zero-to-max tests were conducted by loading both in the concave (compressive) and convex (tensile) configurations. A "failure" was recorded when the component registered resistance above the failure threshold for 10 cycles within 10% of the first failed cycled. Meaning, for example, if the first failure was at 1,000 cycles, the tenth must be ≤ 1,100. The failure threshold resistance used was 5kΩ.

Table 2-2: Durability test matrix.

Loading Amplitude	Overstress test	2.75mm	2.5mm	2.25mm
Compression	1	1	1	1
Tension		1	1	1

2.2.2 Experimental Results

The resulting cycles to failure (N_f) from the 3PT cyclic bend tests are presented in Table 2-3.

Table 2-3: Cycles to failure for 3PT cyclic bend tests, tensile and compressive loadings. Some compressive tests did not complete by the time they needed to be taken offline.

Comp	T225	T250	T275	C225	C250	C275
1	41664	122669	26461	-	-	160864
2	9520	6044	3837	-	137367	9478
3	5510	3114	2873	-	85286	6281
4	96573	87492	6383	-	-	119322
5	71176	30403	13163	-	-	73358
6	6679	5112	3757	-	67740	5230
7	10314	6520	4094	-	100855	10462
8	99306	77325	85119	-	-	-
9	141265	14163	10176	-	110258	56961
10	12355	2822	1870	-	34844	6420
11	9640	4538	3082	-	79260	7390
12	224223	90487	40909	-	-	110823

Destructive failure analysis was conducted on failed specimens. These methods included a process called “Dye & Pry”, as well as standard cross sectioning and lateral polishing.

For the dye and pry process, multiple LGA components, still on the PWB, were covered in a red dying liquid (as seen previously in Figure 2-7) for a few seconds. After being removed from the liquid, a vacuum pump was affixed over the entirety of the LGA specimen on the PWB, activated, and the specimen was gently flexed in order to open any damage sites which exist but are in a closed state when the board

is at rest. The point of the vacuum is to draw the dye in to all the damage sites and crevices exposed to air, in which the dye can seep. After a few minutes the vacuum pump was removed and the specimen is left to dry for about 24 hours. Given that this LGA has a rather large center thermal land, the conventional "pry" part of the process needed to be modified. Since this center thermal land is not of electrical interest, it could be milled out with an end mill. The specimen was milled from the bottom of the PWB to just past the top side of the PWB, in to the solder, to release the center land from the PWB. With this large "anchor" released the rest of the component could be easily pried from the PWB. Finally, under an optical microscope, the existing damage sites show up easily with the dye coloring.

For standard cross sectioning, single LGA components on PWB were again removed from the rest of the PWB as described above. These were then set in an epoxy resin and left to cure overnight. Once solidified, these specimens could be ground down on a grinding wheel, gradually reducing the grit size so as to work toward a smooth cross sectional surface whose only characteristics are, ideally, that of the specimen and not of the grinding. See Figure 2-11.

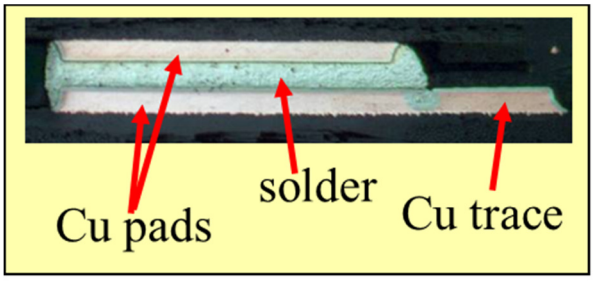

Figure 2-11: Elevational cross-section showing Cu pads, solder, and the beginning of the Cu trace

In some cases, LGA components were desoldered from their PWB footprints directly, and the exposed PWB surface was subjected to lateral polishing. This polishing was done starting with 3um sized powder, since there was only a minimal amount of material (mask and oxidation) to remove from the traces (see Figure 2-12b).

Failure analysis showed that there were no solder failures. The lateral polishing revealed that the most dominant failure mode was fatigue damaging of copper traces emanating from the corner solder pads, just at the edge of the solder mask where the solder joint ends, as shown in Figure 2-12.

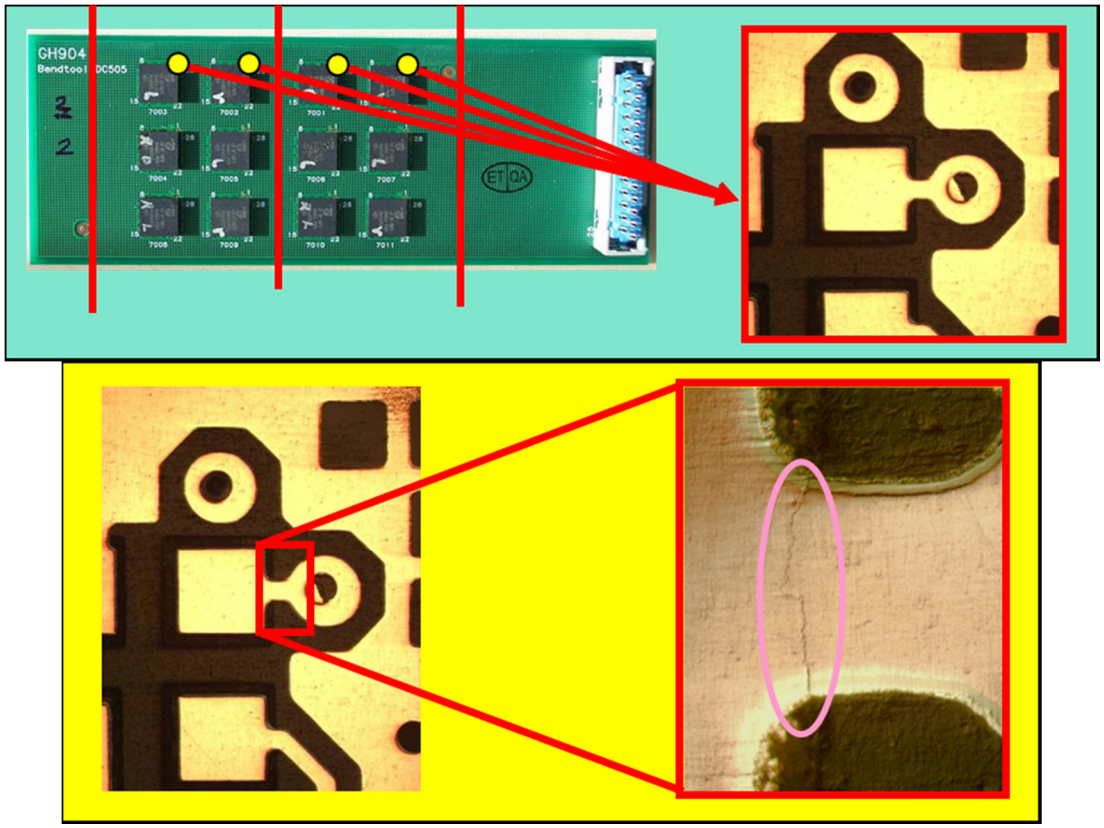

Figure 2-12: (a) Global view of the bend test PWA with Land 1's position noted, with inset showing plan view of laterally polished Land 1 close-up, and (b) Land 1 and the trace attached to it, a zoomed in view showing the fatigue damage across the trace.

Figure 2-13 shows typical 2-parameter (shape and scale parameter) Weibull plots of the failure data separated into the two (inner & outer) groups (tensile only showed here). Figure 2-14 shows each trace configuration separately. From Figure 2-13 it's apparent that the trace configurations should be separated, but Figure 2-14 shows even this starts to break down at the lower load levels. Two-parameter Weibulls were sufficient to describe these data, and the third parameter (location) was not used. The general form of the (3 parameter) Weibull distribution is:

$$F_T(t) = 1 - \exp\left[-\left(\frac{t-\mu}{\eta}\right)^{\beta}\right] \quad t \geq \mu \tag{2-11}$$

When μ = 0, Equation (2-11) becomes the 2 parameter Weibull. In 2002, Alqam et al performed a case study on 26 composite material specimens, comparing reliability estimation using 2 parameter vs 3 parameter Weibull estimations [44]. The conclusion was that 2 parameter was a better choice. Even though the 3 parameter estimation is a more robust formulation, they found statistical and conceptual issues with its use, including the indication that the location parameter implies there are loads below the lower bound such that failure will never occur. Additionally, with an increase in sample size, the advantage of the 3 parameter Weibull formulation could be decreased. With this paper's study, the load levels were varied enough such that it seems reasonable not to try to include a time shift to the Weibull distribution.

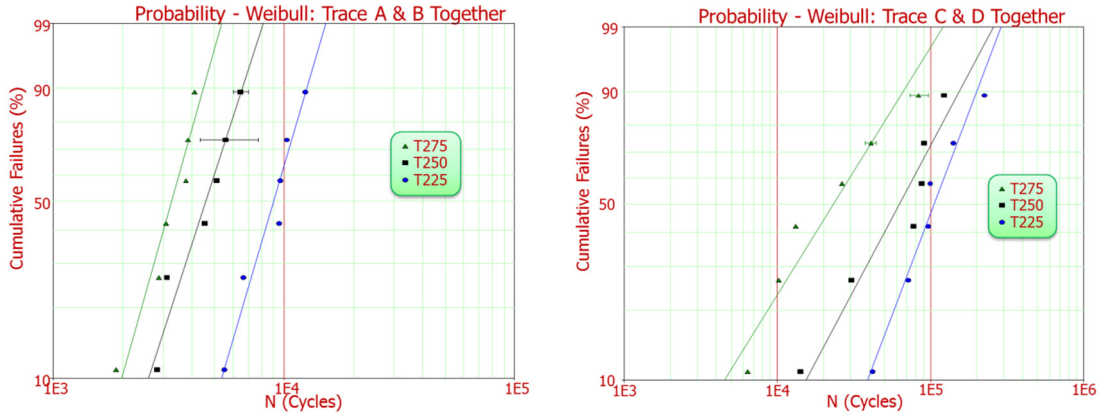

Figure 2-13: 2-parameter Weibull plots of two groups of specimens. The left plot is the inner group (A, B), the right plot is the outer group (C, D).

Table 2-4 shows the Weibull parameter data for the 3PT bend test results. From these data, it can be seen that there is an obvious difference in the fatigue behavior of the outer left and outer right groups, which would be expected to behave similarly if true symmetry was in effect. The variability between inner left and inner right is much less. Because of this separation, the components were then grouped in to four configurations, termed A, B, C, and D. A and B were the two inner groups (columns 2 and 3, respectively, in Figure 2-6), with A being the group with Land 1 closest to the PWA's centerline. C and D were the two outer groups (columns 1 and 4, respectively), with D being the group with Land 1 furthest from the PWA's centerline. Because of this relative location from the centerline, these groups can be quantified by their "L value", which is the distance from the centerline at which the center of the component lies.

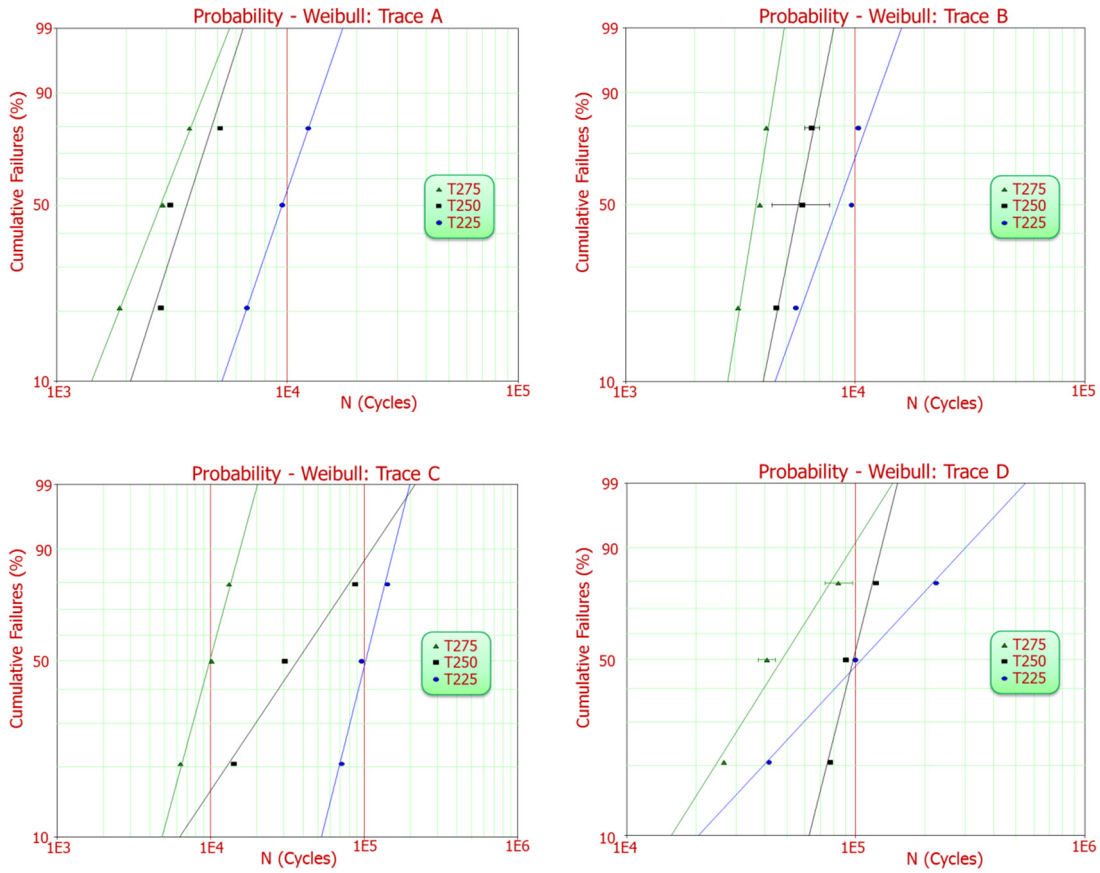

Figure 2-14: 2-parameter Weibull plots of the four groups of specimens. top: inner left (A), inner right (B), outer left (C), outer right (D).

Table 2-4: Weibull parameter results for the 3PT bend test data.

Weibull Constants	T225		T250		T275	
	β	η	β	η	β	η
A & B	3.64	9973	3.30	5133	3.80	3595
C & D	1.88	128290	1.03	74336	1.15	31868
A	3.12	10686	3.36	4074	2.74	3218
B	2.97	9546	5.31	6076	6.64	3905
C	2.84	116390	1.66	26857	2.64	11293
D	1.15	145410	4.16	116760	1.70	588836

The durability results of this test are used later in Section 2.4 of this paper, to derive fatigue S-N curves for the copper material used in the traces, based on detailed FEA assessment of the strain and stress levels at the critical site in the trace.

2.3 Model Simulation

The following section describes the simulation process performed on the model and properties of the 3-point bend experiments to develop the new fatigue model for the Cu trace fatigue life estimation, which is explained in Section 2.4.

2.3.1 Finite Element (FE) Model Development

A "global/local" approach was used to simulate the 3-point bend experiment. A relatively coarse "global" model was used to model the PWA and the loading in the experimental system. Results of this global analysis were harvested to extract the boundary conditions for a "local", much more detailed and finely meshed, sub-model. Many of the details of the PWB structure, e.g. the copper traces, were omitted in the "global" model for computational efficiency, and included in the "local" model instead. The displacements at the boundaries of the local domain were monitored in the global model and applied to the local model as a boundary condition.

The first FE model can be seen in Figure 2-19. This model represents the symmetric right half of the center row of the component. However, this model is representative of the whole PWB because of the periodicity boundary conditions imposed at the edge of this row (representing the center of symmetry for this PWA). The out-of-plane displacement of the bending test is applied as a boundary condition, as shown in Figure 2-6, however there are no in-plane displacement constraints, to mimic the rollers in the test setup and prevent fictitious membrane strains.

As discussed earlier, the traces were not modeled in this simplified global simulation, but the results of this global model were used to inform a local model consisting of just one joint and copper trace, as seen in Figure 2-20. The Cu-trace failure site (at land number 1) was always located in the upper right corner of the component (as shown earlier in Figure 2-12). As discussed earlier, this disrupts the true lateral symmetry of the specimen about the central roller of the bend test, and may explain some of the aberrations in the failure data. To compensate for this asymmetry, four local FEA models were developed, one for each column of components. The corresponding trace configurations and locations, labeled A-D, are seen in Figure 2-19. Each of these lettered locations represents corresponding columns of components in the full test specimen. Letters D, B, A, C in Figure correspond to columns 1, 2 3, 4, respectively, in Figure 2-6.

Both the global and local models were built using ANSYS's eight-noded, 3D structural elements with three degrees of freedom at each node: translations in the x, y, and z directions [45]. Table 2-5 shows the totals for final element and node tallies in both the global and local models, while Table 2-6 shows the linear components of the material models used in the simulations. The constitutive curve for the SAC solder can be seen in Figure 2-15 [46].

Table 2-5: Element and node totals for the global and local 3PT bend test Finite Element Models.

	Global Model	Local CL0	Local CL1	…	Local CL9
Nodes	28162	17187	17187	…	17187
Elements	21722	16435	16432	…	16408

Table 2-6: Linear properties applied to the material models used in the global and local models.

	PWA	SAC	Cu	EMC
E_X (MPa)	25.0E+3	47.5E+3	82.7E+3	11.1E+3
E_Y	25.0E+3			
E_Z	10.0E+3			
ν_{XY}	0.15	0.35	0.35	0.33
ν_{YZ}	0.06			
ν_{XZ}	0.06			
G_{XY} (MPa)	20.0E+3			
G_{YZ}	20.0E+3			
G_{XZ}	15.0E+3			
α_X	15.0E-6	20.9E-6	17.4E-6	13.0E-6
α_Y	15.0E-6			
α_Z	55.0E-6			

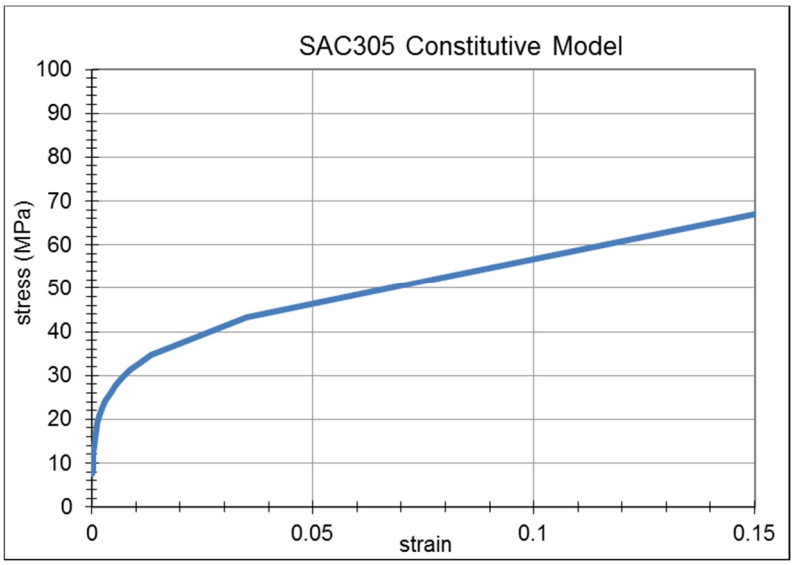

Figure 2-15: Elastic-plastic constitutive curve used to model the SAC solder.

A mesh-convergence study was first run to determine the mesh density that would adequately solve for values which would not be dependent on the mesh density. This was done using ANSYS's "adaptive mesh solver" [45]. For this, only linear properties were used, and the model was only deformed into what the experimentation showed was the linear region. Since the error calculation process compares the average stress at a node and the stress calculated at that node from one of the adjoining elements at a time, the model was also set to one material

overall. The adaptive mesh solver then ran iterations of the load case, revising the mesh each time until convergence is met. This is done by minimizing the "error energy" in the elements selected for the process. The error energy is a volume integral over the stress error vector. This stress error vector is the aforementioned difference between the average value at the node and the value calculated for that node from one of the adjoining elements. Since this model uses length units of mm and stress units of MPa, this gives us error energy units of mJ.

Since the area of interest of this study was only the Cu trace failure site, only that region was selected for improvement. All elements use the same material properties to decrease error in the adaptation.

In 3D models, this adaptive mesh is done using tetrahedral elements (Figure 2-16). Because of this, the exact mesh found using the mesh convergence study was not used, but the relative mesh densities were. The final FE models were built using hexahedral elements (Figure 2-19 and Figure 2-20). In fact, the error energy at the failure site for the *operating* model was only around 0 - 0.5mJ (Figure 2-17).

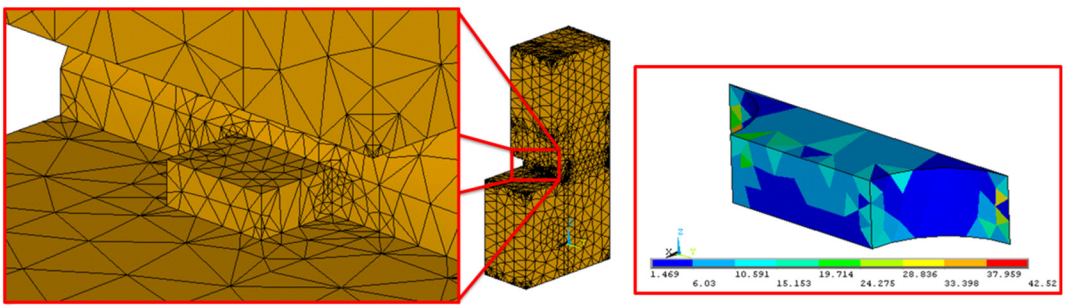

Figure 2-16: Full and multiple insets of the adaptive mesher solved, "converged" mesh density. The contour plot shows the "error energy" of the Cu trace neck up to the failure cross section.

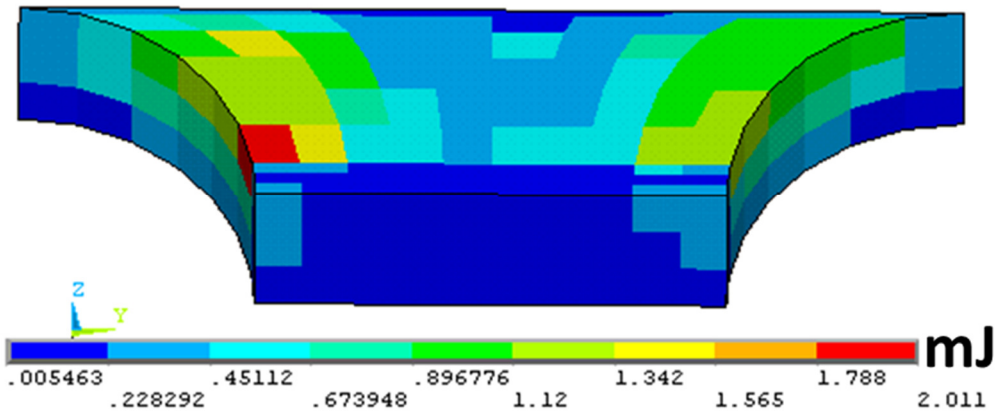

Figure 2-17: Error energy at the failure cross section of the operating local model. The largest error energy occurs at the transition to a new material type, which is inherent in the formulation.

A numeric "per adaptation" plot of the Error Energy as percentage of model energy is shown in Figure 2-18. The error decreases with each adaptation ANSYS performs, starting with a coarse mesh, until the error percentage reaches the predefined threshold of 5% at the selected refinement area. This mesh convergence study operated on the trace.

The load applied to the global model was large enough to achieve 3mm of out-of-plane displacement. Displacements at the boundaries of the "local" domain were monitored during the simulation. The simulation was terminated when the displacements at the moving roller exceeded 3mm. The displacement results of the global simulation were imposed at ten key points of the local model, as displacement boundary conditions. As an example, the resulting x-direction total mechanical strain contours in the local model can be seen in Figure 2-21.

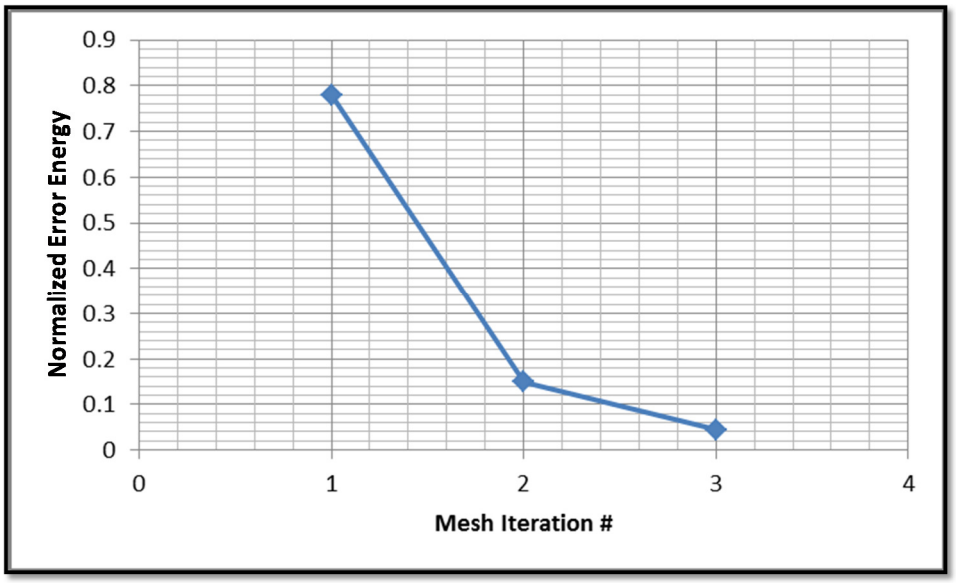

Figure 2-18: Mesh iteration history plot showing the decrease in mesh error.

Using the combined results from the global and local models, a transfer function was developed to relate the observed PWB bending strain (collected from the global model at the same locations where the strain gauges were placed in the experiment) to the average von Mises' strain experienced by the Cu trace. The strain in the trace is averaged over the critical cross-section that experiences fatigue failure using a "volume-weighted average" in case there are any non-uniformities between elements. The volume-weighted average is found by first finding the fraction of the total cross-section's volume that belongs to the element. Next, the centroidal value of the results data of interest is multiplied by this volume fraction. This sum of each of these for all the elements of the region being investigated gives the volume-weighted average. Examples of the strain transfer functions from the strain gauge value to this calculated Cu trace neck value can be seen in Figure 2-22.

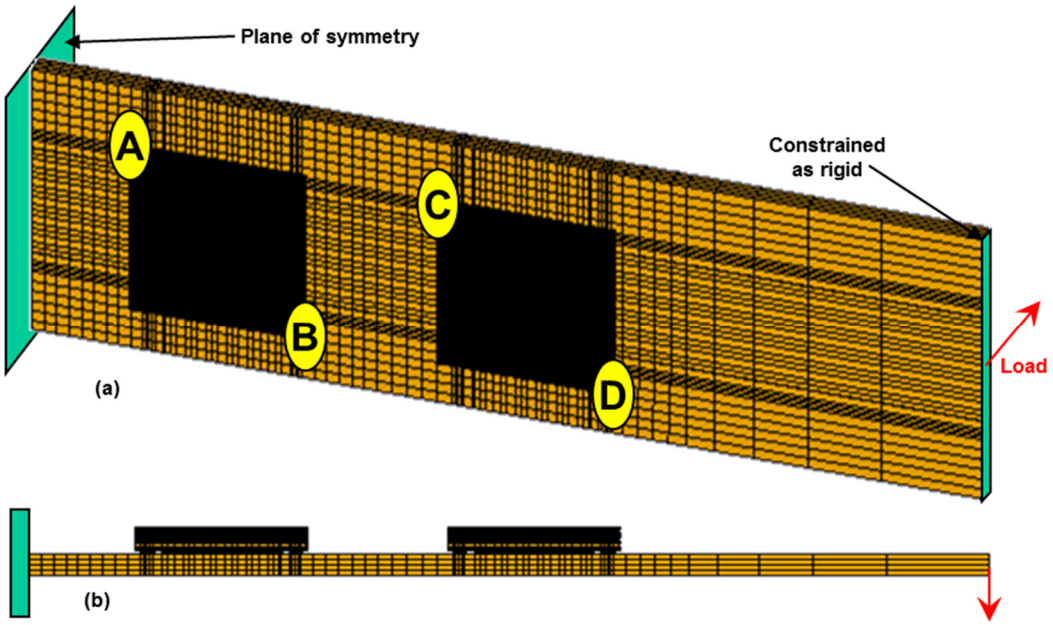

Figure 2-19: Global FE model of inner and outer component.
(a) Oblique view showing the locations where the BCs for each of the different trace regions were found. "A" is components 3/6/10, "B" is components 2/7/11, "C" is components 4/5/9, and "D" is components 1/8/12; and (b) elevation view.

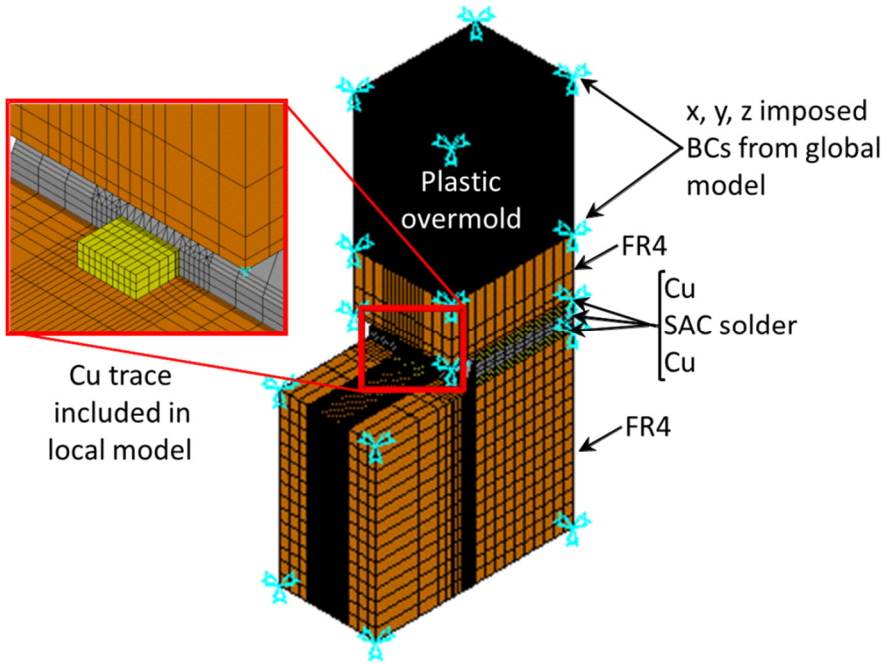

Figure 2-20: Local model of single joint with added Cu trace emanating from the Cu land.

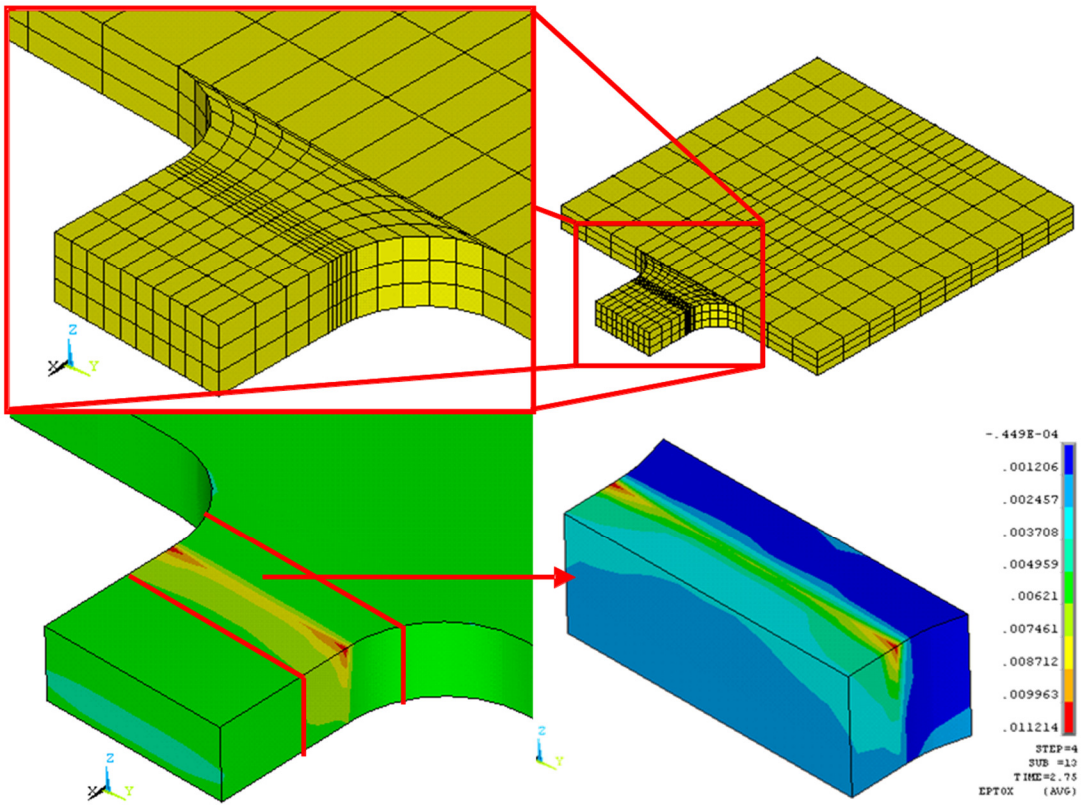

Figure 2-21: CCW from top-right, this shows Cu land number 1, a closer view of the land, the x-direction strain contours in the zoomed view, and the more precise strain contours of just the neck region where the fatigue damage occurs.

Using these transfer functions, Cu trace strains in the critical neck were inferred from measured PWB bending strain for all the loading and geometric configurations. The FEA local model was exercised for two full cycles and the cyclic history of the averaged von Mises strain in the copper trace were recorded. Generally, the cyclic strain ranges do not stabilize until the second or third cycles. This model was determined to stabilize by the second. The cyclic range of the second cycle was recorded and can be found in Table 2-9 for a selected set of copper trace properties, alongside the Response Surface results that will be discussed in Section 2.3.4.

The cyclic strain range in the copper trace shown in Table 2-9, was combined with the measured fatigue life of Table 2-3, to develop S-N curves for the Cu traces.

Clearly, the cyclic strain range in the copper, estimated from the FEA transfer function, depends on the elastic-plastic stress-strain behavior input into the FEA model for the electro-plated copper. Due to the large uncertainty in these properties in the literature mentioned earlier, the elastic-plastic constitutive properties of copper and a compatible set of S-N fatigue curves are iteratively determined together, from the failure data. In-house copper stress-strain data (shown in Figure 2-23) is used as an initial estimate of the stress-strain curves for Cu, to start this iteration process. Since key properties were found to vary rather linearly with changes in the K value of the Ramberg-Osgood material model (Equation (2-1)) for the Cu, a "Response Surface" (RS) which will be explained in Section 2.3.3, was set up using the simulation results.

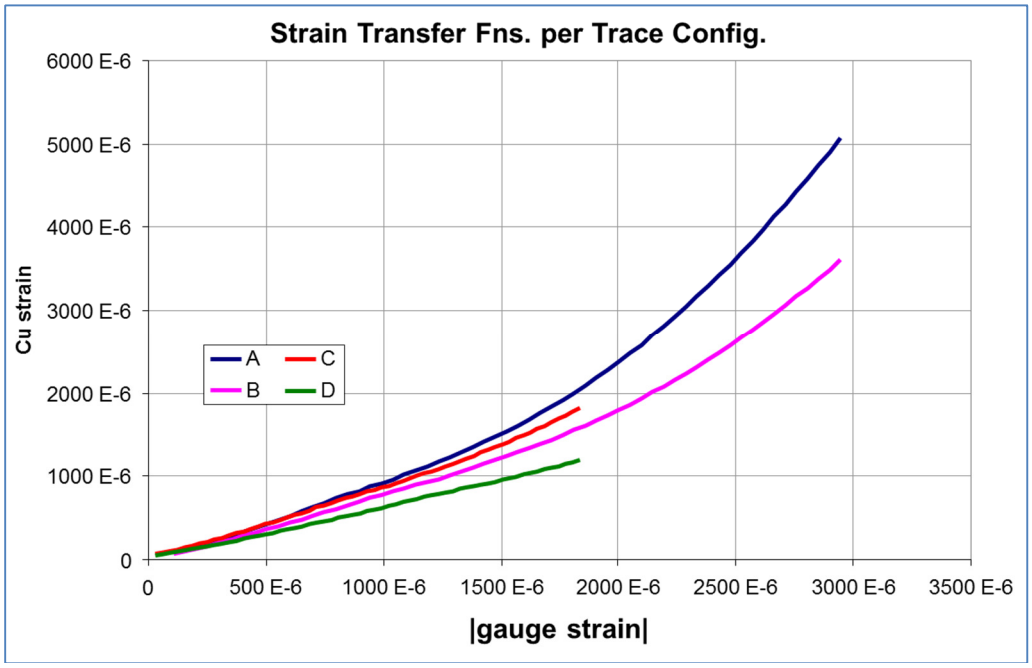

Figure 2-22: Strain transfer functions for tensile 3-point loading. There are four (4) curves corresponding to each joint location type, seen in Figure 2-19.

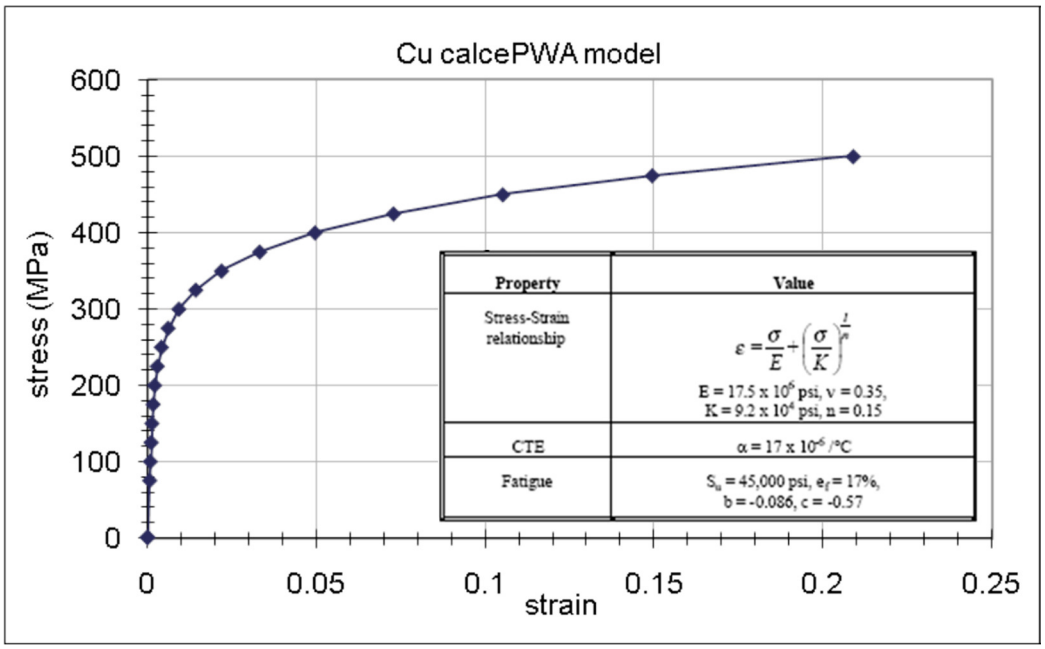

Figure 2-23: Initial Cu model used, inset showing the material model table from the calcePWA [47] software database including constitutive model constants and corresponding fatigue constants.

2.3.2 Simulation Results

The global and local models' deformed geometries can be seen in Figure 2-24. Further detailed deformed geometry of the Cu trace neck area with accompanying total equivalent strain contours can be seen in Figure 2-25.

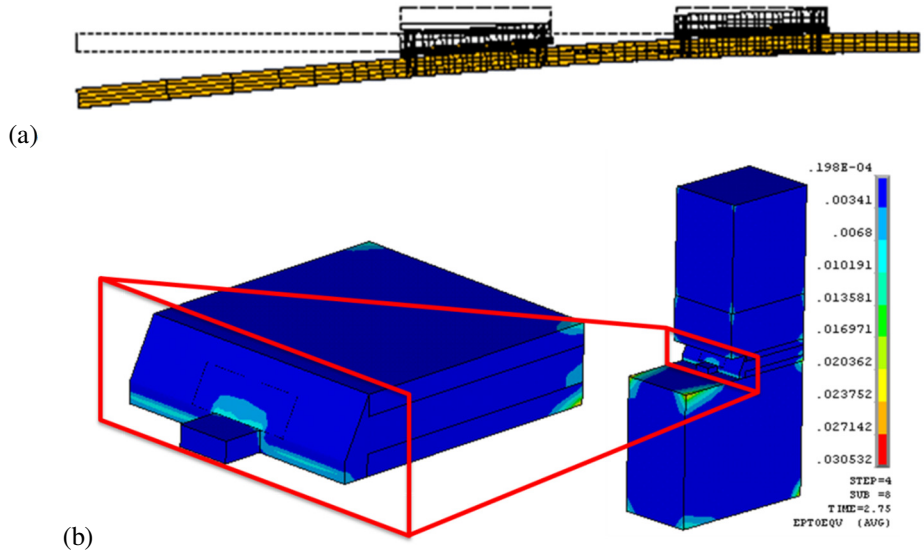

Figure 2-24: Deformed geometry of the (a) global, elevation view with undeformed edge and (b) local, EPTO (ANSYS notation for EPsilon TOtal) contours FE models.

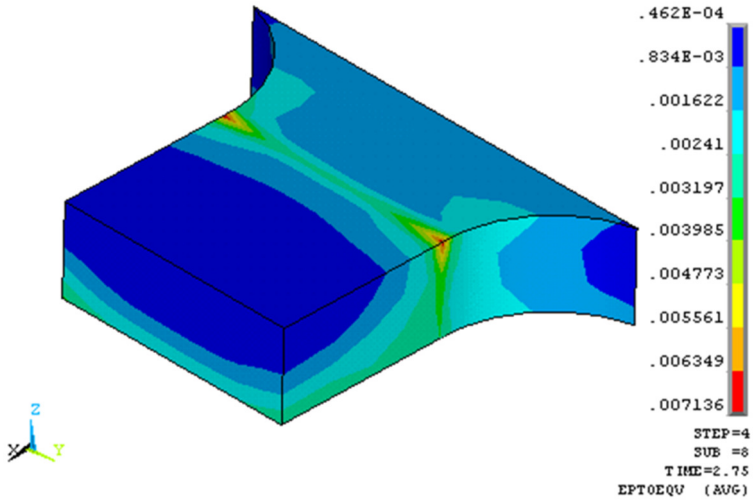

Figure 2-25: Close up of the deformed geometry of the Cu trace neck of a sample trace/loading configuration, with total equivalent strain contours.

Preliminary simulations showed that when the K value of the Ramberg-Osgood material model (Equation (2-1)), the L value, or the deflection load was changed for the FE model, the resulting data from the simulation showed that the equivalent elastic strain, equivalent plastic strain, and hydrostatic pressure all varied reasonably piecewise linearly in kind for the extreme trace configurations and loadings (trace A

load 275 and trace D load 225). Since for each iteration of fitting σ'_f and ε'_f involves a new material model, which means new 3PT bend simulations to find new results to put in to the fatigue model to fit new σ'_f and ε'_f, for each of the 12 trace and loading configurations, the computation time needed bordered on untenable. So three landmark K-value simulations were run and the results were collected to form the RS explained in the next section. These values were K=56.5, K=100, and K=200. The results data varied linearly from 56.5 to 100, and from 100 to 200, as can be seen in Figure 2-26.

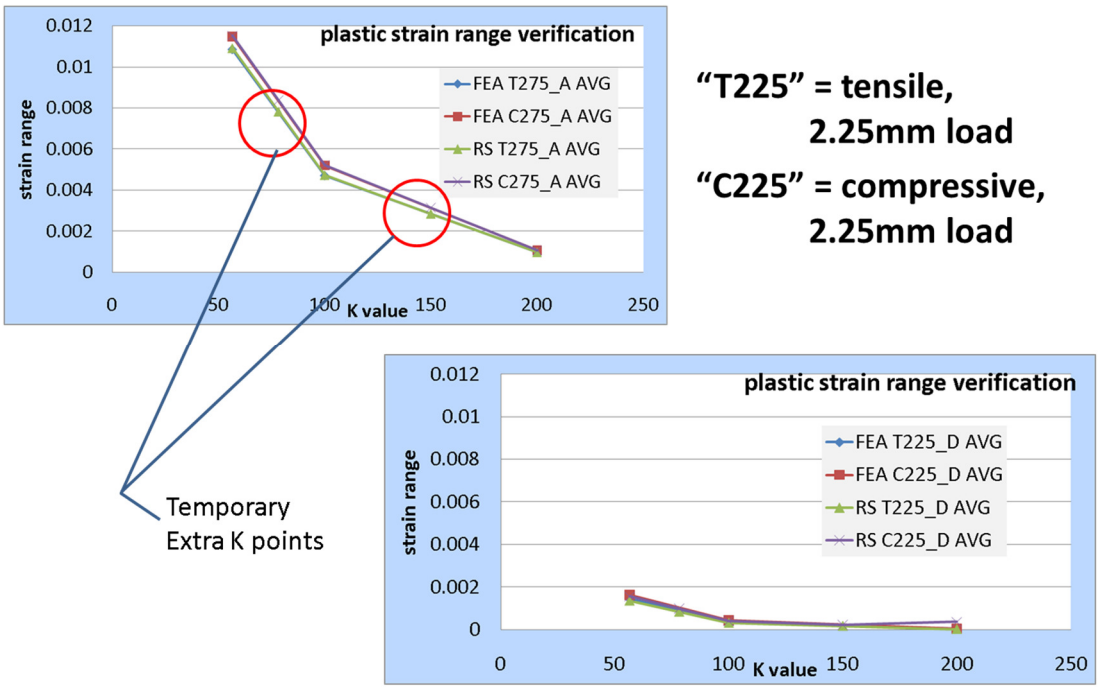

Figure 2-26: Plastic strain range results from trace A, deflection 2.75mm (A275) and trace D, deflection 2.25mm (D225) showing linearity of results.

2.3.3 Response Surface (RS) Development

With the results from the previous section, a Response Surface was developed. This way, a system of linear equations could be solved nearly instantaneously instead of a lengthy process of iterations of finite element simulations.

First, a program called NLREG was used to find the constants for each response surface. The general equation of the response surface is:

$$RS = C0 + C1 \cdot K + C2 \cdot L + C3 \cdot \delta + C4 \cdot L^2 + C5 \cdot KL + C6 \cdot K\delta + C7 \cdot L\delta + C8 \cdot KL\delta + C9 \cdot L^2\delta + C10 \cdot KL^2 + C11 \cdot KL^2\delta \quad (2\text{-}12)$$

where K is the value from the Ramberg-Osgood material model (Equation (2-1)) in MPa, L is the distance of the component's center from the PWA centerline in mm, δ is the load in mm of deflection, and "RS" is the response surface quantity which is either plastic strain, elastic strain, or hydrostatic pressure. The L value is of second order since these quantities are more sensitive to the distance from the PWA centerline, and this sensitivity can give added accuracy. Since the configurations are piecewise linear from K=56.5 to K=100 and then from K=100 to K=200, two response surfaces were developed for each configuration. With a total of four trace configurations (or "L values"), three loadings (or "δ values"), both tensile and compressive bend test data, and two response surfaces for each configuration, that's a total of 12 response surfaces for 36 model configurations. All Response Surfaces are of the form of equation (2-12). The constants for each of the 12 (six compressive and six tensile) can be seen in Table 2-7 and Table 2-8.

Table 2-7: Constants C0 through C11 for equation (2-12) for compressive data for linear sections 1 and 2.

	Compressive RS Constants used to solve for:					
	$\varepsilon_{elastic}$ 1	$\varepsilon_{elastic}$ 2	$\varepsilon_{plastic}$ 1	$\varepsilon_{plastic}$ 2	σ_H 1	σ_H 2
C0	92.36 E-6	-685.66 E-6	3.79 E-3	2.59 E-3	-23.94 E+0	-62.41 E+0
C1	-1.03 E-6	6.75 E-6	-25.28 E-6	-13.21 E-6	-13.15 E-3	371.50 E-3
C2	10.81 E-6	159.92 E-6	-635.52 E-6	-209.34 E-6	1.87 E+0	1.46 E+0
C3	67.34 E-6	1.10 E-3	-3.45 E-3	-1.51 E-3	10.08 E+0	10.12 E+0
C4	-152.08 E-9	-3.33 E-6	9.95 E-6	-1.45 E-6	-29.97 E-3	1.60 E-3
C5	136.60 E-9	-1.35 E-6	5.43 E-6	1.17 E-6	-18.83 E-3	-14.66 E-3
C6	782.81 E-9	-9.53 E-6	27.48 E-6	8.01 E-6	-86.52 E-3	-86.93 E-3
C7	-4.87 E-6	-98.94 E-6	423.95 E-6	98.28 E-6	-728.96 E-3	177.43 E-3
C8	66.10 E-9	1.01 E-6	-3.85 E-6	-596.77 E-9	9.52 E-3	456.04 E-6
C9	58.41 E-9	1.83 E-6	-2.58 E-6	2.52 E-6	10.66 E-3	-10.15 E-3
C10	-564.21 E-12	31.24 E-9	-113.06 E-9	940.75 E-12	333.97 E-6	18.26 E-6
C11	-770.43 E-12	-18.48 E-9	43.23 E-9	-7.72 E-9	-146.48 E-6	61.71 E-6

Table 2-8: Constants C0 through C11 for equation (2-12) for tensile data for linear sections 1 and 2.

	Tensile RS Constants used to solve for:					
	$\varepsilon_{elastic}$ 1	$\varepsilon_{elastic}$ 2	$\varepsilon_{plastic}$ 1	$\varepsilon_{plastic}$ 2	σ_H 1	σ_H 2
C0	537.60 E-6	-239.02 E-6	5.38 E-3	1.31 E-3	42.35 E+0	-58.41 E+0
C1	-7.57 E-6	198.33 E-9	-46.50 E-6	-5.79 E-6	-784.57 E-3	222.99 E-3
C2	-15.26 E-6	60.41 E-6	-696.18 E-6	-137.12 E-6	-2.96 E+0	5.77 E+0
C3	-79.59 E-6	352.91 E-6	-3.90 E-3	-1.02 E-3	-15.21 E+0	28.76 E+0
C4	227.50 E-9	-943.54 E-9	9.44 E-6	-1.94 E-6	46.06 E-3	-103.52 E-3
C5	510.01 E-9	-246.68 E-9	6.27 E-6	681.77 E-9	60.62 E-3	-26.68 E-3
C6	2.90 E-6	-1.42 E-6	33.92 E-6	5.14 E-6	295.78 E-3	-143.88 E-3
C7	3.78 E-6	-23.37 E-6	423.62 E-6	71.63 E-6	1.03 E+0	-2.44 E+0
C8	-56.89 E-9	214.54 E-9	-3.93 E-6	-410.28 E-9	-20.53 E-3	14.16 E-3
C9	-66.15 E-9	343.65 E-9	-2.08 E-6	2.48 E-6	-15.32 E-3	41.10 E-3
C10	-5.97 E-9	5.74 E-9	-107.76 E-9	6.01 E-9	-904.05 E-6	591.84 E-6
C11	988.73 E-12	-3.11 E-9	36.86 E-9	-8.79 E-9	298.81 E-6	-265.45 E-6

These equations can all be solved instantly. MATLAB was used. Table 2-9 shows the comparison of RS values and FEA values for equivalent plastic strain. Each color set in Table 2-9 is data set for a different K value (56.5, 100 or 200). The top group is the plastic strain data mined from the FEA model, and the bottom group is that produced by the Response Surface. For example, the data points for Figure 2-26 came from the "2.75" lines of each color / K value, in the first column, which is trace A, and the last column, which is trace D.

Table 2-9: Cyclic minima and maxima of Cu trace plastic strain, from FEA and from RS using the milestone K values in MPa used to develop the RS.

EPPL

TIME	K = 56.5_FEA_A_EPPL	K = 56.5_FEA_B_EPPL	K = 56.5_FEA_C_EPPL	K = 56.5_FEA_D_EPPL
2.25	0.007865	0.005669	0.002935746	0.00144569
2.75	0.010847	0.007978	0.004419509	0.002267086

TIME	K = 56.5_RS_A_EPPL	K = 56.5_RS_B_EPPL	K = 56.5_RS_C_EPPL	K = 56.5_RS_D_EPPL
2.25	0.007932084	0.005461081	0.003122274	0.001364039
2.75	0.010922685	0.007745757	0.004630534	0.002176637

TIME	K = 100_FEA_A_EPPL	K = 100_FEA_B_EPPL	K = 100_FEA_C_EPPL	K = 100_FEA_D_EPPL
2.25	0.00311	0.002072	0.00090897	0.000344047
2.75	0.004702	0.003193	0.001497823	0.000631921

TIME	K = 100_RS_A_EPPL	K = 100_RS_B_EPPL	K = 100_RS_C_EPPL	K = 100_RS_D_EPPL
2.25	0.003127422	0.00198333	0.0009819	0.000313309
2.75	0.004730038	0.003074334	0.001600973	0.000590335

TIME	K = 200_FEA_A_EPPL	K = 200_FEA_B_EPPL	K = 200_FEA_C_EPPL	K = 200_FEA_D_EPPL
2.25	0.000600696	0.000340412	0.000095582	0.000022907
2.75	0.000961674	0.000563142	0.000186205	0.000050834

TIME	K = 200_RS_A_EPPL	K = 200_RS_B_EPPL	K = 200_RS_C_EPPL	K = 200_RS_D_EPPL
2.25	0.000600554	0.000319875	0.000112233	1.61494E-05
2.75	0.000963666	0.000536565	0.000208938	4.18922E-05

2.3.4 RS Results

A MATLAB algorithm was developed to iterate and converge on a K value for the Cu model that is calculated using the monotonic values of the best fitting σ'_f and ε'_f for the resulting cross sectional strains and hydrostatic pressures that result from the Cu model, with the experimental cycles-to-failure (N_f). This algorithm used a nonlinear fitting technique that would back calculate the necessary fatigue and empirical constants needed to satisfy the fatigue model in use, which can be seen in Equations (2-13) and (2-14) and is described in the next section.

2.4 Fatigue Model Development

The cyclic mean stress must be used since the cyclic bend tests were not fully reversed, meaning they were a “zero to max” bend test instead of a “-max to +max” bend test. This causes a “mean stress effect” since the stress is oscillating about a nonzero value. In standard fatigue relation formulations, some relation of the mean stress and fatigue strength (σ'_f) constant are used for the mean stress effect factor.

In this study's case, the von Mises equivalent from which the fatigue strength constant is found can be dwarfed by the hydrostatic pressure at the Cu trace's fracture site. Because of this, the standard fraction of mean stress divided by fatigue strength is not sufficient. Once this fraction becomes greater than one, the relation breaks down. A hyperbolic tangent function was applied as a limiter, since $\tanh(x) \to 1, \text{ for any } x > 1$, The function then simply tends toward the low cycle fatigue (LCF) term as the mean stress surpasses the fatigue strength.

A generalized strain-life power-law model, corrected for the average hydrostatic stress at the failure site, is used to describe the fatigue durability of the Cu material, as shown below in Equation (2-13), if one is using an unbounded compressive strength (UCS). The bounded compressive strength (BCS) model is shown in Equation (2-14), where i=1 for tensile and i=2 for compressive loading. The physical appropriateness of these two models is still contested in the fatigue field [48-50]. The BCS model holds that there is a certain compressive strength at which the life cycle benefit saturates, hence "bounded". The UCS model holds that theoretically the benefit to life keeps increasing as compressive cyclic mean stress increases. For this study, the question of UCS or BCS is not addressed, however both options are presented. In the case of the UCS model, the standard modified Morrow fatigue model see in Equation (2-8), is used for the compressive cyclic mean stress. There are obvious advantages to the UCS or BCS models. The differences can be seen in Figure 2-27. The further away from a stress ratio of 0, the more these differences matter. At extreme compressive mean stresses, the difference between BCS and UCS

will certainly matter. In Chapter 3, the extreme case in this study will be discussed; large tensile mean stresses which enunciate the difference between the standard Sines model and the BCS/UCS developed in this study.

$$\frac{\Delta\epsilon}{2} = \begin{cases} \frac{\sigma'_f}{E}\left[1 - \tanh\left(\frac{m_1 \cdot \sigma_m}{\sigma'_f}\right)\right](2N_f)^b + \epsilon'_f(2N_f)^c, & \sigma_m \geq 0 \\ \frac{\sigma'_f}{E}\left[1 - \frac{m_2 \cdot \sigma_m}{\sigma'_f}\right](2N_f)^b + \epsilon'_f(2N_f)^c, & \sigma_m < 0 \end{cases} \quad (2\text{-}13)$$

$$\frac{\Delta\epsilon}{2} = \frac{\sigma'_f}{E}\left[1 - A_i \cdot \tanh\left(\frac{m_i \cdot \sigma_m}{\sigma'_f}\right)\right](2N_f)^b + \epsilon'_f(2N_f)^c \quad (2\text{-}14)$$

Here $\Delta\epsilon$ is the total strain range in a cycle, σ'_f is the cyclic failure stress, E is the elastic modulus, ε'_f is the cyclic failure strain, and N_f is the cycles-to-failure. The model constants were estimated by fitting this model to the measured cycles-to-failure of Table 2-3, using a least-square regression scheme.

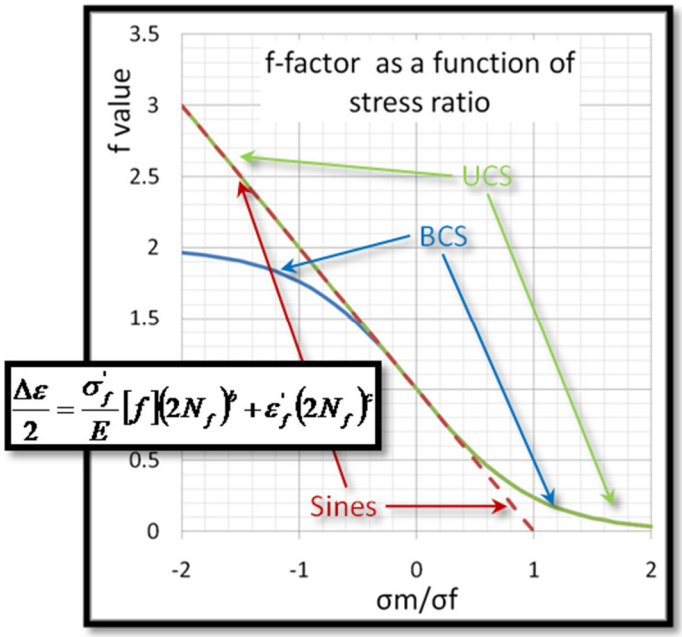

Figure 2-27: Generalized plot of the effect of the mean stress correction or "f" factor. The dotted line is the Morrow model which treats the correction linearly. The BCS curve shows a saturation

level in compression and tension while the UCS model applies Morrow in compression and a saturation in tension.

As discussed above, the model constants are determined iteratively, along with the mechanical elastic-plastic constitutive properties, starting with the initial model constants available from earlier in-house studies of PTH fatigue. The overview is described in Figure 2-28 while the details of the "MATLAB AFCs Solver" box can be found in Figure 2-29. The final result of this iteration is shown in Figure 2-30. The term "AFC" is shorthand for "Average cross section Fatigue Constants". This is to distinguish them from the "IFCs" or "Incremental cross section Fatigue Constants" which will be described in the next chapter.

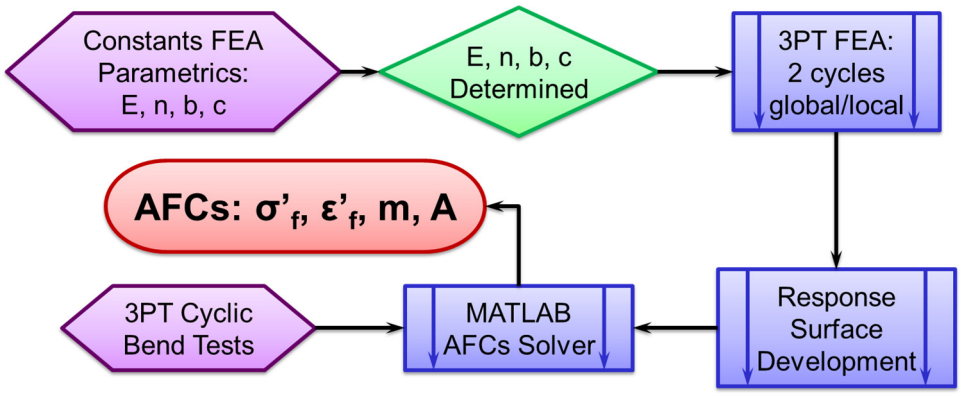

Figure 2-28: Flowchart of the full cross section model constant development process.

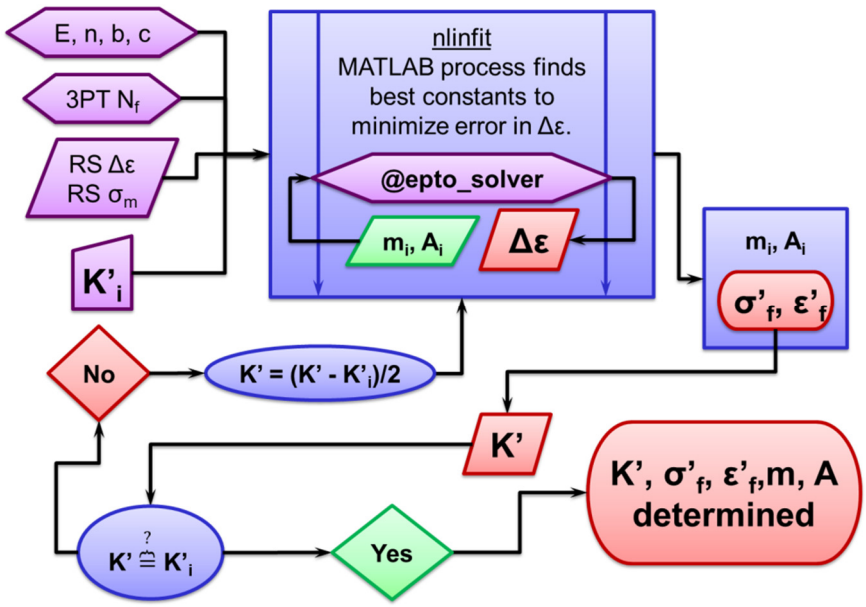

Figure 2-29: Detail flowchart of the MATLAB process used to iteratively solve for K and the AFCs; the box labeled "MATLAB AFCs Solver" in Figure 2-28.

Since some of the model constants in the fatigue model are related to those in the stress-strain model constants, iteration was needed to match the S-N model constants to the stress-strain curve, as discussed above in the beginning of the chapter.

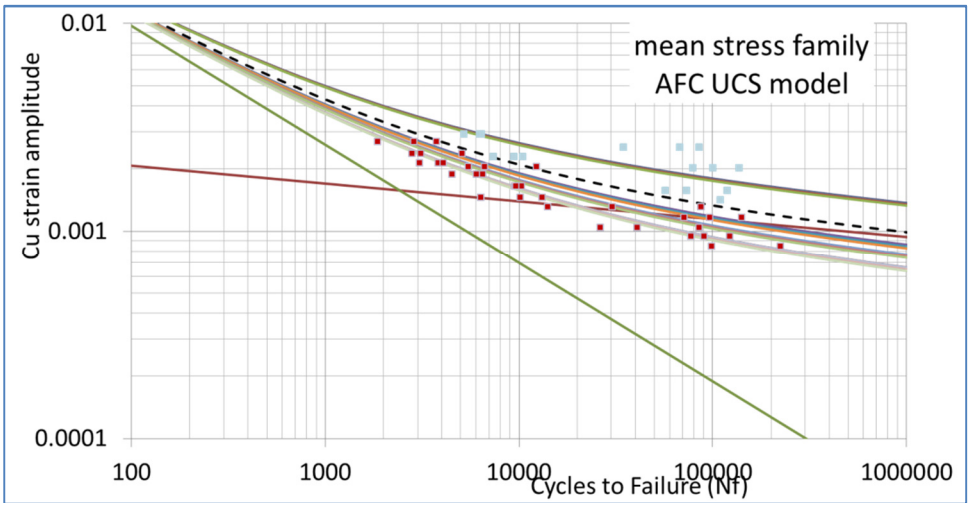

Figure 2-30: Damage model incorporating the high cycle fatigue Basquin curve and the low cycle fatigue Coffin-Manson curve, with the "tanh" ratio limiter. This is the fatigue curve fit to the Cu trace failure data based on the average strain in the trace cross section.

As a check, the plots of N_f predicted v N_f observed for the AFCs are shown in Figure 2-31. The R^2 value of the correlation is 77%.

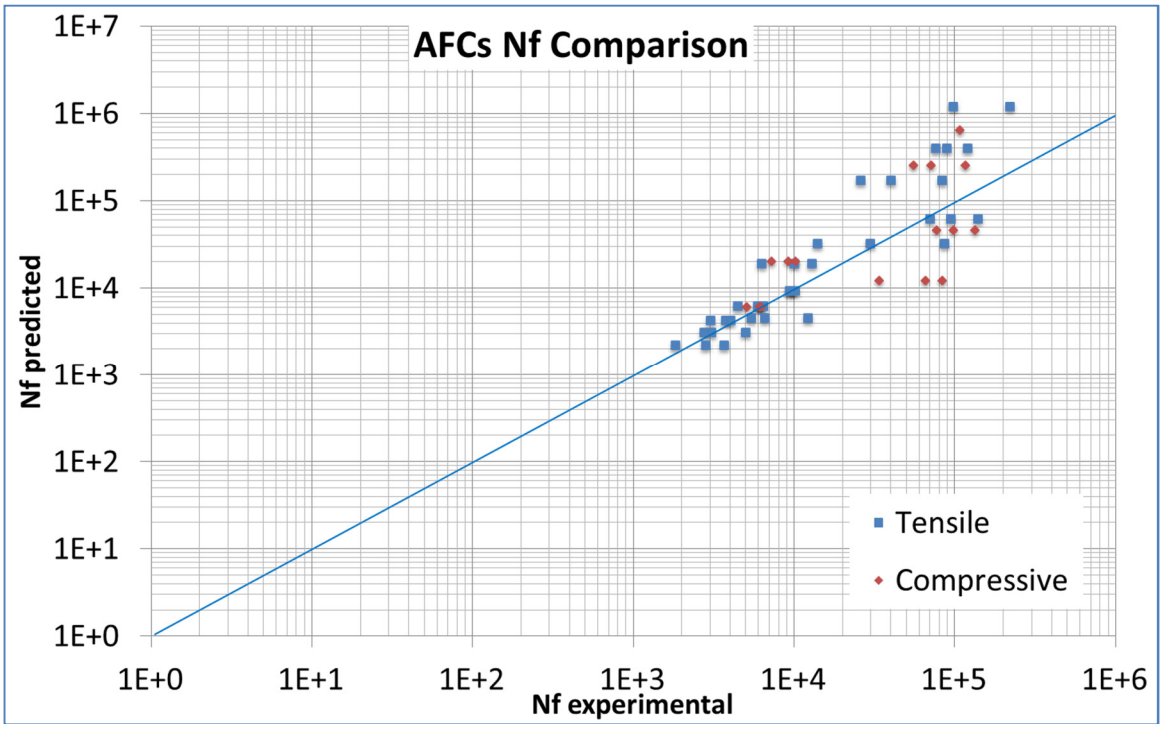

Figure 2-31: Comparison plot of predicted life vs observed life, with a y=x line drawn for clarity.

2.5 Summary

This paper has presented the results of cyclic fatigue durability testing of daisy-chained PWAs under quasi-static bending. Failure analysis revealed that the failures were due to fatigue damage initiation and propagation in the Cu traces. The fatigue life of the Cu traces was investigated using finite element models, response surfaces, and the experimental data, along with the inter-related material model.

Fatigue constants for a fatigue model that forces a saturation of the mean stress effect on the tensile side of the spectrum were calculated (BCS) as well as for a model with no compressive stress life benefit (UCS). Although m_i and A_i constants were accounted for, they tended toward a value of 1 each in the end. The BCS model

for the AFCs predicted a fatigue strength of 134.7MPa and an elongation of 10%, which is on the low end of the expected material model outcome. The UCS model for the AFCs predicted a fatigue strength of about the same as the BCS model. The constants predicted by the UCS and BCS models are found in Table 2-10 and Table 2-11. The constitutive constants are shown in Table 2-12. These were the K values solved simultaneously with the fatigue constants to best fit the results. The data in red in all three tables are data that were held fixed.

Table 2-10: Final BCS model fatigue constants.

fatigue (BCS)	
b	-0.086
c	-0.571
ε_f	10%
σ_f (MPa)	134.66
m_1	1
m_2	1
A_2	1

Table 2-11: Final UCS model fatigue constants.

fatigue (UCS)	
b	-0.086
c	-0.571
ε_f	10%
σ_f (MPa)	134.66
m_1	1
m_2	1

Table 2-12: Final constitutive model constants from AFC method.

constitutive	
n	0.150
K_{mono} (MPa)	222.9
K_{cyclic} (MPa)	190.7

Chapter 3: Incremental Fatigue Damage Model based on Local Strain

This chapter investigates separately the initiation and the propagation of fatigue damage in copper traces under flexural loads, using an incremental form of the fatigue model developed in the last chapter. The previous chapter considered the total fatigue damage and did not attempt to distinguish between the initiation and propagation. This results in incremental fatigue constants (IFCs) and is done by using 10 separate models for each combination of trace configuration and load level investigated. The difference between these 10 models is that each has a successive discrete section of the failure cross section removed, to simulate a growing damage region. This approach is intended to simulate the actual damage propagation more closely than a simple average cross section strain range loading profile. The incremental continuum damage method is preferred over a fracture mechanics approach because it is more suited to the distributed damage seen over discrete local regions of the microstructure, rather than a straight, mathematically sharp crack.

Before the revised incremental fatigue model constants are presented, a review of the previous steps is included. This includes the baseline 3pt cyclic bend tests, the development of the fatigue model used, the average cross-section fatigue constants (AFCs), and the FE models used in this study.

This incremental analysis is used not only to provide more accurate fatigue initiation constants based on the local strain (as opposed to average strain over the cu-trace cross-section), but also to shed important insights into the relative magnitudes of the initiation period and the propagation period for different loading magnitudes.

3.1 Introduction

This section of the thesis investigates the development of a fatigue model for the failure of Cu based on the immediate local strain at the leading edge of the fatigue damage region. This is done using a process termed "Successive Initiation" (SI), which can be likened to using Riemann sums to estimate an integral value as opposed to actually calculating the full integral.

3.1.1 Problem Statement

Often in the assessment process for electronics, time is of the essence. Of course, in all of engineering, there must be a decision made between the trade-offs of increased accuracy and swiftness of an answer. The Incremental cross-section Fatigue Model and its constants (IFCs) seek to assess the fatigue life of a Cu trace using the physics of continuum damage initiation and propagation, rather than fracture mechanics. The incremental continuum damage method is preferred over a fracture mechanics approach because it is more suited to the distributed damage seen over discrete local regions of the microstructure, rather than a straight, mathematically sharp crack.

3.1.2 Background & Motivation

In the previous chapter, a fatigue model was developed for the Cu traces on a PWA situated beneath solder joints. This model was developed using a "snapshot", if you will, of the trace's cross sectional strain range from the second bending cycle. This concept is boiled down to one value of strain for the entire cross section. These constants were termed "AFCs", for Average Cross-section Fatigue Constants.

In this chapter, the intent is to improve upon this model's accuracy by building up the complexity considered at the Cu trace's cross section. By this, it is meant that instead of as before, assessing the full cross section of the trace and determining when its strain level reaches a failure point based on the material model and the fatigue constants, a small discrete section of the cross section will be assessed. After this section is determined to reach failure, a next discrete section of equal size will be assessed, and so on. This process continues until a cumulative damage index (CDI) is developed and used to calculate the cumulative cycles to failure of each section based on the cycles it experiences when it's not the leading edge and the strain it experiences when it is the leading edge.

The key to this chapter is found in Figure 3-1. This ESEM image shows the morphology of the failure site of the Cu traces. The damage is seen to meander around the grain boundaries, much like some cracks, however the width of the damage is different. This is not a mathematically sharp, straight crack. Hence fracture mechanics is not the best approach to qualify and quantify the failure

behavior. Also noticeable is how the damage propagation becomes unstable at around 70% of the trace width. This will be discussed later, in Section 3.4.

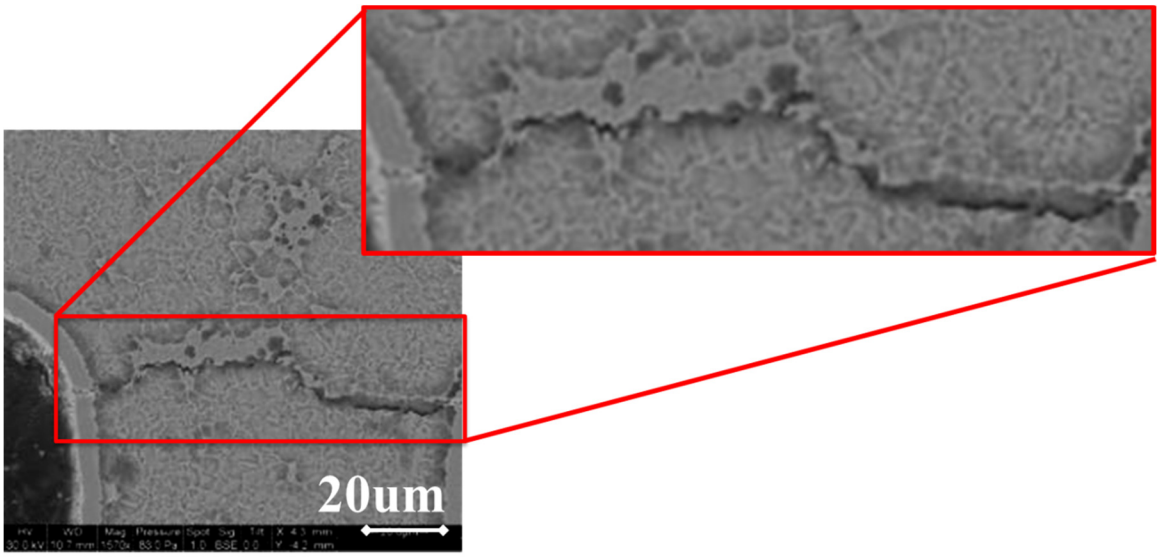

Figure 3-1: ESEM image of the damage zone in a tensile loading Cu trace specimen. The path and surrounding details of the damage points toward not a standard, straightforward crack but rather a meandering zone of microstructural damage distributed over a local zone of finite width.

There are of course benefits to both the AFC and IFC method. The IFCs can be used when a material model is already known, since there is much more work involved if the constitutive model is not yet determined. However, using the AFC method of last chapter, it can be seen that both the fatigue constants and the corresponding constitutive model can be found simultaneously. But the AFC method is also more geometry-specific. Since the method is fit to a whole cross section average, very different cross sections could yield different results. The IFC model, as will be explained in this chapter, is based on incremental sections of the cross section failing at a time and is therefore much more discrete and geometry independent.

3.1.3 Literature Review

When assessing the mechanical durability of electronic assemblies, the dominant failure site is generally believed to be in the solder interconnect [13]. However, in many package styles, such as BGAs (ball grid arrays), LGAs (land grid arrays), MLFs (micro lead frame) and QFNs (quad flat no-lead), the Cu trace emanating from the solder pad may be the weakest failure site, especially if the solder joint is copper-defined rather than mask-defined, and if there is a sudden neck with sharp re-entrant corners where the copper trace emanates from the solder pad [12, 14, 15]. This is particularly true in situations with cyclic mechanical loading, such as cyclic quasi-static bending, vibration and repetitive drop/shock [5, 9, 10, 12-14].

3D multitechnology, multi-functional, multichip packaging technology, usually referred to as a "SiP" (system-in-package), has emerged as one of the leading methods of miniaturization. These packages can be found anywhere miniaturization is needed, from portable electronics, to smart biomechanical implants, Micro-Opto-Electromechanical Systems (MOEMS), biochemical 'lab-on-a-chip' sensors, and even home appliance electronic controls [7, 8]. Additionally, these packages frequently forego leads and even solder balls for further miniaturization. This generally results in stiffer, more robust solder interconnects. Consequently, the mechanically weakest point in the chain becomes the traces on the PWA [9-14].

This paper investigates the cyclic stress and strain histories in the Cu traces and attempts to quantify the accumulated fatigue damage in terms of these parameters.

Prior research by the authors had focused on the solder interconnects for this package style [18, 19]. In the present study the focus is on the Cu traces.

The literature reveals many examples where the Cu trace is the weakest point in the system and the dominant failure site [11, 12]. Additionally, these failures have been found to be easily preventable by revision to the trace design. Studies show that redesigned Cu traces can indeed survive repetitive mechanical loading and that the failure site shifts elsewhere [11, 13, 20, 21].

Quantitative insights are needed into the fatigue durability of copper traces so that failures can be predicted and design guidelines can be developed to prevent these failures. The existing literature does not have a consensus of Cu properties for electronics devices [22-25]. The decision was made to use Engelmaier's E_{Cu} and n_{Cu}. Engelmaier's work using E = 82.7GPa [22, 23] has been used most, and falls in the middle of the field as far as the literature goes.

Okura's method of "successive initiation" (SI) is adapted in this chapter [51]. In his study, Okura used the SI method to predict the damage propagation path in two dimensional models of void-free flip-chip solder joints. Later, Ladani modified the approach for three dimensional models, for her work with solder joints that did have voids [52]. Ladani's model used the Energy Partitioning fatigue model.

3.2 Summary of Experimental Results: 3PT Cyclic Bend Tests

The following section is a brief summary of the material presented in the previous chapter, describing the 3PT bend tests used for this study

3.2.1 Specimen & Test Methodology

The package of interest in this study is an RF SIP component for use in portable electronic products. It contains multiple wirebonded dice, flip-chip dice, and ceramic SMD passives, all on a common substrate. The wirebonded dice are attached to the laminate board with die attach. There are no die stacks in this SiP. The package is fairly stiff because of the many components molded together on a multi-layer substrate and has an LGA architecture, which includes interconnection pads along the perimeter, and a large thermal land in the center.

The PWA specimen used in this study were JEDEC (Joint Electron Devices Engineering Council) standard bend test boards and set in a standard 3-point flexure setup. Non-functional daisy-chained components are used, with corresponding daisy chains in the PWB, to facilitate electrical failure monitoring.

The geometry and loading of this specimen are symmetric about the center roller. The stress levels are highest in the interconnects of the inner columns, followed by those of the outer columns. Although the components are located symmetrically with respect to the center roller, Land 1 locations are asymmetric since they are located at the top right corner of each component. Thus the local curvature at Land 1 is different for each column, generating 4 different loading levels in each bend test.

In this test set-up, the center roller imposes out-of-plane cyclic movement from zero to max. Since the loading is zero-to-max (R=0) and not completely reversed (R=-1), tests are conducted with PWAs facing both directions in the fixture. Thus, in some

tests the interconnects experience convex curvature (tensile loading) and in some they experience concave curvature (compressive loading).

During the actual testing phase, first overstress tests to determine the destruct limits of the test specimen. Next, failure analysis to determine the dominant failure modes in the overstress tests. Third, the selection of AST (accelerated stress test) levels that are below the destruct limits, do not cause failure mechanism shifting, and are sufficiently severe to produce timely failures was done. Finally, tests and analysis to characterize the specimen response to the entire range of excitations anticipated in the accelerated stress test were done.

To characterize the specimen for mechanical cycling, a populated test board was subjected to overstress loading, instrumented with strategically placed strain gauges. The overstress tests showed that a deflection amplitude of about 3mm was sufficient to fail interconnects within the first few mechanical cycles and the force-deflection curve remained linear within the 3mm deflection envelope, so the amplitudes for cyclic testing were therefore kept under 3mm.

Cyclic fatigue testing was performed next. Eight test boards, populated with 12 components each were subjected to 3 different load levels, or "δ values" to generate sufficient data points on the S-N curve. A "failure" was recorded when the component registered resistance above the failure threshold for 10 cycles within 10% of the first failed cycled. Meaning, for example, if the first failure was at 1,000 cycles, the tenth must be ≤ 1,100. The failure threshold resistance used was 5kΩ.

3.2.2 Experimental Results

Failure analysis showed that there were no solder failures. The lateral polishing revealed that the most dominant failure mode was fatigue damaging of copper traces emanating from the corner solder pads, just at the edge of the solder mask where the solder joint ends.

Because of a separation in the failure data, the components were grouped in to four configurations, termed A, B, C, and D. A and B were the two inner groups, with A being the group with Land 1 closest to the PWA's centerline. C and D were the two outer groups, with D being the group with Land 1 furthest from the PWA's centerline. Because of this relative location from the centerline, these groups can be quantified by their "L value", which is the distance from the centerline at which the center of the component lies.

3.3 Review of Prior Work

The previous chapter included the Finite Element model strategy leading to the developmental process of the average cross sectional fatigue constants and their fatigue model. The process is summarized here for the reader's convenience.

3.3.1 FEA Global-Local Model

The FEA strategy in this study was to use the global-local modeling system. In this approach, a global model of the experimental system at-large is run, which in turn informs the boundary conditions imposed on a much smaller and computationally intricate local model of the failure site of interest.

In simulating the 3PT cyclic bend test, a global model consisting of two representative components on their respective PWA areas were used. Using symmetry, this model was loaded to capture the behavior of all four trace configurations found to exist in the experimental phase. Displacement data from strategic locations surrounding the corner land, "Land 1", were collection and applied as the boundary conditions of the local model. The local model consisted of this Land 1 and the PWA all the way through to the other side under its footprint, below it; and the solder and corresponding component land and everything about that, as well as a portion of the emanating Cu trace and the PWA beneath it. The same local model, structurally, could be used for each of the four trace configurations, with different displacement boundary conditions being applied accordingly.

3.3.2 Fatigue Model Development

The cyclic mean stress must be used since the cyclic bend tests were not fully reversed, meaning they were a "zero to max" bend test instead of a "-max to +max" bend test. This causes a "mean stress effect" since the stress is oscillating about a nonzero value. In standard fatigue relation formulations, some relation of the mean stress and fatigue strength (σ'_f) constant are used for the mean stress effect factor. In this study's case, the von Mises equivalent from which the fatigue strength constant is found can be dwarfed by the hydrostatic pressure at the Cu trace's fracture site. Because of this, the standard fraction of mean stress divided by fatigue strength is not sufficient. Once this fraction becomes greater than one, the relation

breaks down. A hyperbolic tangent function was applied as a limiter, since $\tanh(x) \to 1,$ for any $x > 1$, The function then simply tends toward the low cycle fatigue (LCF) term as the mean stress surpasses the fatigue strength.

3.3.3 Failure Analysis

Three different types of failure analyses were used on the failed specimens of the 3pt cyclic bend tests: traditional cross-sectioning, lateral polishing, and "dye & pry".

The first method used was standard cross sectioning. Since this study began as another assessment of solder failures, this is where the focus was, initially. No damage could be found, however, in the solder, Cu trace, or PWA using traditional cross sectioning.

The second method used was dye & pry. For this method, the specimens were dipped in an indelible dye and vacuum sealed briefly, while being deflected so that they dye had a chance to seep in to any and all damaged regions which may exist on the exposed areas. The vacuum sealing served the purpose of further aiding the seepage of dye by drawing it in to crevices. After this, the components were removed from the PWAs, and set under optical microscopes. In the case of damaged regions, the dye serves to make more pronounced their existence, to aid in detection. No damage was found using this method either.

The third method used was lateral polishing. For lateral polishing, the components are removed immediately. The solder is then wicked away using heat and solder wick ribbons. Since all that is now left is some solder remainder and mask and

surface impurities on the Cu traces and lands, a very light polishing was applied to the surface of the PWA on the component's footprint. Using this method, multiple damaged regions were found on the Cu traces. All of which were found at the failure site investigated in this study.

3.3.4 AFC Development Study

Recall from the previous chapter that the AFCs were developed using, at once, the full cross section of the Cu trace. The von Mises equivalent total strain range and the cyclic mean stress for the second simulated bend cycle are fed in to a MATLAB solver. The MATLAB solver fits the best set of constants to the fatigue relationship using the experimental cycles-to-failure as the "N_f".

A generalized strain-life power-law model, corrected for the average hydrostatic stress at the failure site, is used to describe the fatigue durability of the Cu material if one is using an unbounded compressive strength (UCS) or bounded compressive strength (BCS) model. For this study, the relative advantages of UCS or BCS are not addressed, however both options are presented. In the case of the UCS model, the standard modified Morrow fatigue model is used for the compressive cyclic mean stress.

The model constants are determined iteratively, along with the mechanical elastic-plastic constitutive properties, starting with the initial model constants available from earlier in-house studies of PTH fatigue. The model constants were estimated by fitting this model to the measured cycles-to-failure of the experiments, using a

least-square regression scheme. Since some of the model constants in the fatigue model are related to those in the stress-strain model constants, iteration was needed to match the S-N model constants to the stress-strain curve.

3.4 Successive Initiation Method for Continuum Damage Propagation

This next section describes the method used to improve upon the AFC fatigue model methodology.

3.4.1 FEA Cyclic Model Results for Successive Initiation

Much like the process of development of the AFCs, this process began with finite element simulation. In fact, the FE simulations for the AFC process are each the first of 10 successive models that needed to be run for each trace and loading configuration permutation. These are examples of "damage zone length zero" (DL0) models.

The Cu trace cross sections, in the FE model, had 30 elements in an arrangement of three elements across the height of the trace and 10 elements across the width of the trace. Each of those ten sets of 3 were considered a discrete length of the damage zone. So, for example, for the second model of the series, "damage zone length one" or DL1, the first column of three elements was removed and the local model was solved again, using the same boundary conditions for two bend cycles. Next, DL2 was run, and so on up to DL9. For graphical examples, see Figure 3-2. This was done for each of the four trace configurations, three load levels, and two load types, totaling 4×3×2×10 = 240 simulations.

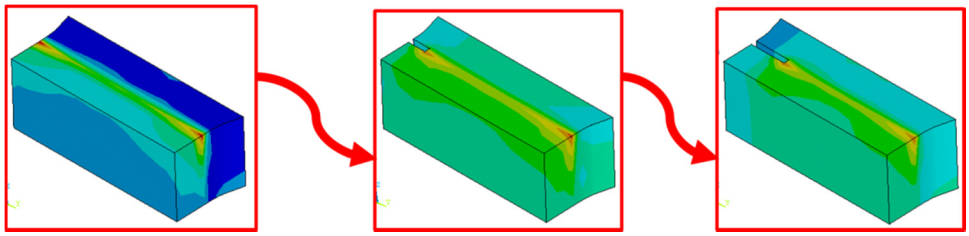

Figure 3-2: Cu trace sections of the first three SI models showing damage zone lengths 0, 1, and 2.

Each of the 240 simulations were post processed to mine the von Mises equivalent strain range and cyclic mean stress experienced by each element at the cross section, if it still existed. The three elemental values for each column were averaged together to give one value per cross sectional column.

3.4.2 Incremental Fatigue Constants (IFCs)

The stress and strain data needed for the MATLAB code to solve for the damage and eventually life were mined into charts like the example in Table 3-1. This chart's first line is the average of each of the 10 columns across the cross section, three elements each. The second line is from the CL1 model where, as it can be seen, the first column no longer exists. This continues until CL9. The strains are then used to calculated (MATLAB algorithm found in the Appendices) discrete N_fs, as seen in Table 3-2, for each cell of Table 3-1. These Discrete N_fs are then compiled in to cumulative asset of Damage per Cycle, Table 3-4. Cumulative N_fs, Table 3-3, are calculated using each cell's previous row's values of Total Damage and current values of Damage per Cycle, while the Total Damage (Table 3-5) cells are solved using that row's leading edge Cumulative N_f and the current Damage per cycle. Finally, the Total N_fs (Table 3-6) are calculated using the previous row's Total N_f and the current row's leading edge Cumulative N_f.

Table 3-1: Trace A, T275 example table showing the strain data collected from all SI models for a given trace configuration and loading profile.

discrete EPTO from FEA	column 1	2	3	4	5	6	7	8	9	10
1	0.004251	0.002625	0.002256	0.002117	0.002184	0.002165	0.002126	0.002327	0.002669	0.004241
2	0	0.006303	0.002285	0.002311	0.002224	0.002213	0.002155	0.002358	0.002696	0.004275
3	0	0	0.006958	0.00248	0.002588	0.002315	0.002242	0.002428	0.002753	0.004359
4	0	0	0	0.007171	0.00286	0.002742	0.002377	0.002564	0.002855	0.004501
5	0	0	0	0	0.008082	0.003021	0.002882	0.002755	0.003037	0.00471
6	0	0	0	0	0	0.00848	0.003206	0.003317	0.003259	0.005052
7	0	0	0	0	0	0	0.009068	0.003614	0.003926	0.005474
8	0	0	0	0	0	0	0	0.009729	0.004407	0.006559
9	0	0	0	0	0	0	0	0	0.012008	0.007476
10	0	0	0	0	0	0	0	0	0	0.021602

Table 3-2: Example table showing the discrete Nfs calculated from the above Table 3-1.

discrete Nfs (from MATLAB)	column 1	2	3	4	5	6	7	8	9	10
0	470	1260	1700	3100	3050	3090	3120	1650	1250	480
1	0	220	2180	1550	2870	2920	2990	1610	1230	470
2	0	0	190	1870	1300	2620	2050	1520	1180	460
3	0	0	0	180	1480	1160	1830	1370	1110	440
4	0	0	0	0	160	1320	1040	1200	990	410
5	0	0	0	0	0	150	920	830	870	370
6	0	0	0	0	0	0	140	740	610	330
7	0	0	0	0	0	0	0	120	530	240
8	0	0	0	0	0	0	0	0	80	200
9	0	0	0	0	0	0	0	0	0	30

Table 3-3: Example table showing the Cumulative Nfs calculated for A_T275

Cumulative Nfs	column 1	2	3	4	5	6	7	8	9	10
0	470	1260	1700	3100	3050	3090	3120	1650	1250	480
1		138	1577	1315	2428	2476	2540	1151	768	10
2			125	1420	1037	2098	1647	957	604	-125
3				125	1038	873	1358	749	450	-240
4					99	852	701	547	290	-340
5						86	533	310	168	-396
6							68	200	58	-429
7								21	-9	-362
8									-5	-319
9										-47

Table 3-4: Damage per Cycle calculated for AA_T275

Damages per Cycle	column 1	2	3	4	5	6	7	8	9	10
0	2.13E-03	7.94E-04	5.88E-04	3.23E-04	3.28E-04	3.24E-04	3.21E-04	6.06E-04	8.00E-04	2.08E-03
1		4.55E-03	4.59E-04	6.45E-04	3.48E-04	3.42E-04	3.34E-04	6.21E-04	8.13E-04	2.13E-03
2			5.26E-03	5.35E-04	7.69E-04	3.82E-04	4.88E-04	6.58E-04	8.47E-04	2.17E-03
3				5.56E-03	6.76E-04	8.62E-04	5.46E-04	7.30E-04	9.01E-04	2.27E-03
4					6.25E-03	7.58E-04	9.62E-04	8.33E-04	1.01E-03	2.44E-03
5						6.67E-03	1.09E-03	1.20E-03	1.15E-03	2.70E-03
6							7.14E-03	1.35E-03	1.64E-03	3.03E-03
7								8.33E-03	1.89E-03	4.17E-03
8									1.25E-02	5.00E-03
9										3.33E-02

Table 3-5: Total Damage calculated for A_T275

Total Damage	column 1	2	3	4	5	6	7	8	9	10
0	1	3.73E-01	2.76E-01	1.52E-01	1.54E-01	1.52E-01	1.51E-01	2.85E-01	3.76E-01	9.79E-01
1		1.00E+00	3.40E-01	2.41E-01	2.02E-01	1.99E-01	1.97E-01	3.71E-01	4.88E-01	1.27E+00
2			1.00E+00	3.08E-01	2.99E-01	2.47E-01	2.58E-01	4.53E-01	5.94E-01	1.55E+00
3				1.00E+00	3.83E-01	3.55E-01	3.26E-01	5.44E-01	7.07E-01	1.83E+00
4					1.00E+00	4.29E-01	4.21E-01	6.26E-01	8.06E-01	2.07E+00
5						1.00E+00	5.14E-01	7.29E-01	9.05E-01	2.30E+00
6							1.00E+00	8.21E-01	1.02E+00	2.51E+00
7								1.00E+00	1.06E+00	2.60E+00
8									1.00E+00	2.57E+00
9										1.00E+00

Table 3-6: Total N_fs for each discrete damaged segment to fail.

Total Cycles	column 1	2	3	4	5	6	7	8	9	10
0	470	470	470	470	470	470	470	470	470	470
1		608	608	608	608	608	608	608	608	608
2			733	733	733	733	733	733	733	733
3				858	858	858	858	858	858	858
4					957	957	957	957	957	957
5						1042	1042	1042	1042	1042
6							1110	1110	1110	1110
7								1132	1132	1132
8									1127	1127
9										1080

The benefits can be seen in Figure 3-3. Here, the two horizontal lines are the N_f predicted using the RS from the AFCs (top line) and the SN_f (scaled N_f) which is just a linear scaling of the N_f value by the initiation to propagation ratio (IPR). The curved line is the line plotted by the values in Table 3-6 against the distance across the trace width. Notice the line peaks between 70-80% across the width. This correlates with the previous ESEM image of Figure 3-1. In Figure 3-1 can be seen physical evidence of the damage zone reaching instability, like the peak of the curve in Figure 3-3.

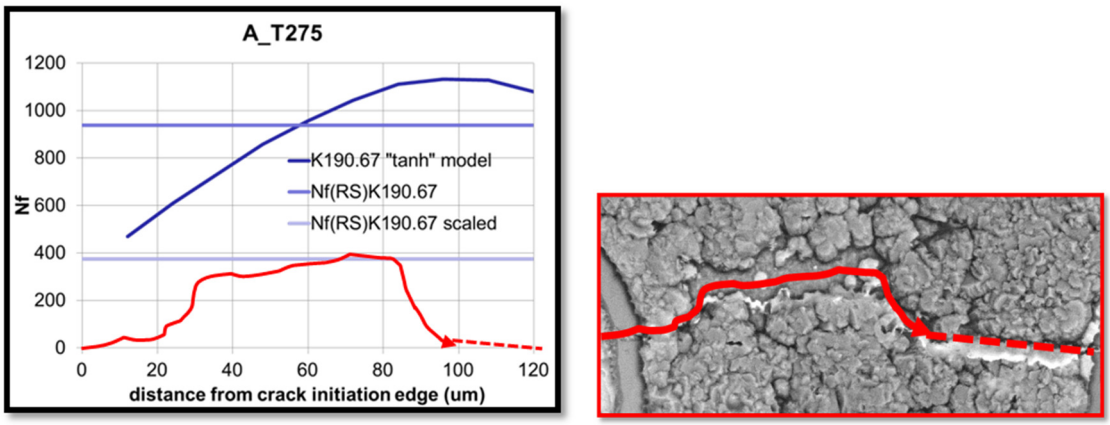

Figure 3-3: Plot of TNfs across the trace width for a K value of 190.67MPa using the tanh model. Overlaid on the plot is the fatigue damage path, also highlighted over an ESEM image, seen at the right.

The fatigue model that results can be seen in Figure 3-4. This figure is similar to that found in the chapter on AFC development, however both cycles to initial or first failure (SN_f) and total cycles to failure (TN_f) are included. The strain axis is now only the strain range to initiation since the rest of the stages grow in to a table of values instead of the singular EPTOi.

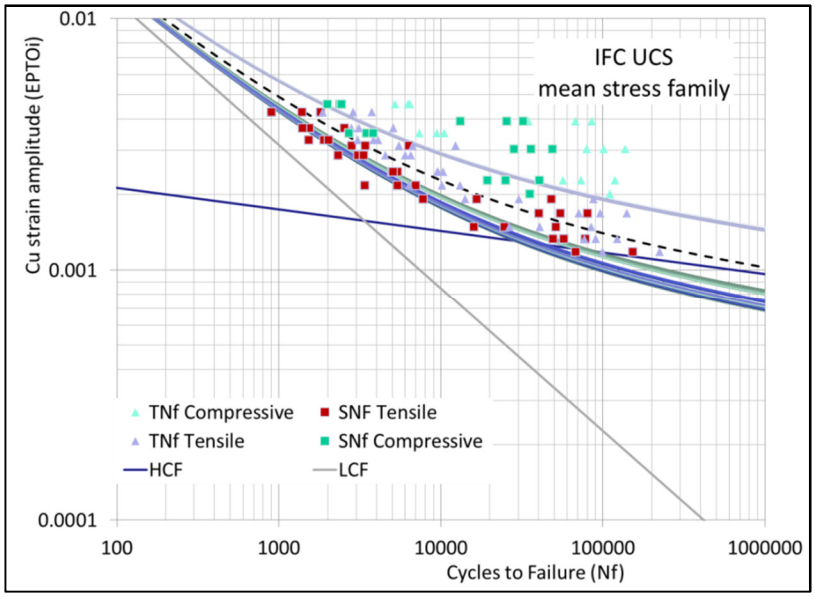

Figure 3-4: IFC UCS fatigue model showing failure data (TNf) and initiation data (SNf). The dotted line is the zero mean stress curve, and the rest of the lines pertain to a certain mean stress level for a failure data point. The EPTO on the t-axis is the initial strain found in the leading column of the DL0 model.

As a check, the plots of N_f predicted v N_f observed for the IFCs are shown in Figure 2-31. The R-squared value of the correlation is 71%. The two plots in Figure 3-6 and Figure 3-7 show two interesting relationships: IPR vs a certain strain ratio and IPR vs a certain stress ratio.

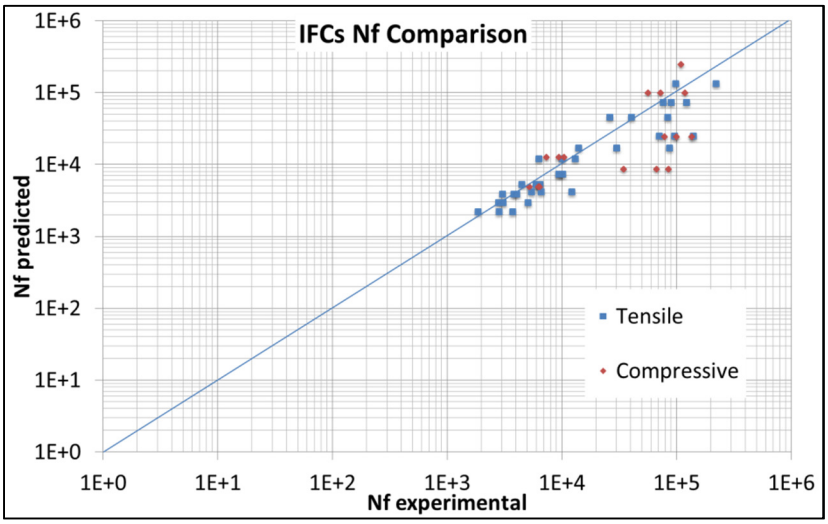

Figure 3-5: Comparison plot of predicted life vs observed life, with a y=x line drawn for clarity.

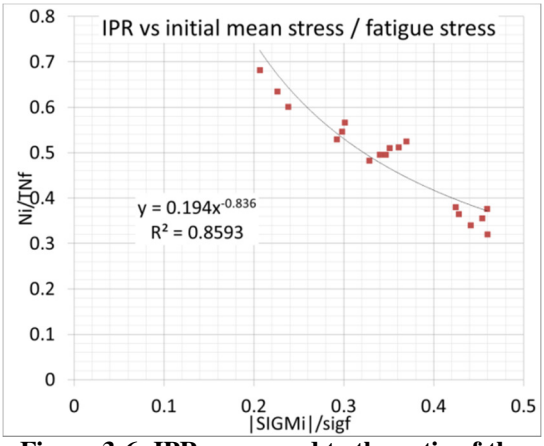

Figure 3-6: IPR compared to the ratio of the mean stress in the first damaged zone segment to the fatigue strength.

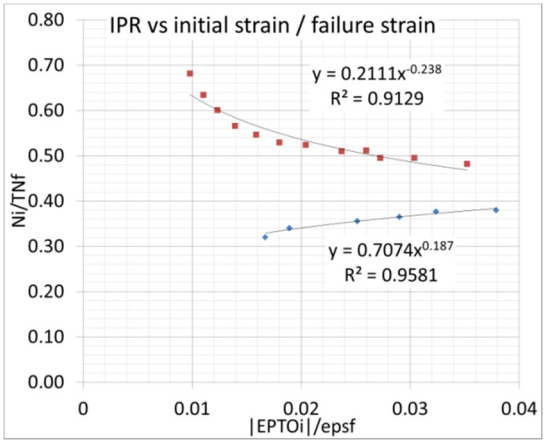

Figure 3-7: IPR compared to the ratio of the strain range in the first damaged zone segment to the fatigue ductility.

3.5 Summary & Discussion

This chapter has presented a further advancement upon the previous chapter's AFC fatigue model. For the development of the IFCs, each AFC model was taken as

"damage zone length zero" (DL0) and subsequent models were made of DL1, DL2, etc. This was done by eliminating the next column of three elements along the front of the damaged zone as the failure progressed across the cross section. All told, 240 models were run, the data mined, collected, and compiled to base a fatigue estimation on a more precise estimation on what goes on at the failure site. For this IFC model, the damaged zone is assumed to successively initiate at discrete stages until full failure, instead of simply assessing the strain and mean stress at the full cross section and determining the fatigue life from there.

Both models are equally valid, but the IFC model presented here offers more accuracy by accounting separately for the time the damage zone will take to initiate vs the time it will take to propagate to failure. The closer to a value of one that the initiation/propagation ratio becomes, the closer together the estimates of the AFC and IFC models will be. In this study, the ratios for each trace and load configuration permutation were around 50 to 65% for the tensile loads and around 40% for the compressive loads.

Although the constants of m_i and A_i were allowed in the IFC model, as they were in the AFC model, they again tended toward a value of 1 for all of them. The BCS model predicted a fatigue strength of 141.7MPa with a corresponding elongation of 14%, which lies right around Engelmaier's numbers [22, 23]. The UCS model predicted a fatigue strength of 138.6MPa with a corresponding elongation of 12%. The constants predicted by the UCS and BCS models are found in Table 2-10 and

Table 2-11. The constitutive constants, which were kept the same as were found in the AFC model, are repeated in Table 2-12.

Table 3-7: Final BCS model fatigue constants.

fatigue (BCS)	
b	-0.086
c	-0.571
ε_f	14%
σ_f (MPa)	141.66
m_1	1
m_2	1
A_2	1

Table 3-8: Final UCS model fatigue constants.

fatigue (UCS)	
b	-0.086
c	-0.571
ε_f	12%
σ_f (MPa)	138.55
m_1	1
m_2	1

Table 3-9: Final constitutive model constants from AFC method.

constitutive	
n	0.150
K_{mono} (MPa)	222.9
K_{cyclic} (MPa)	190.7

Chapter 4: Cu- Trace Fatigue Model: Case Study and Parametric Guidelines

This chapter demonstrates a case study, where the two fatigue modeling methodologies developed for copper traces, in Chapters 2 and 3 from 3-point cyclic bend tests on land grid array (LGA) assemblies, are verified against another independent data-set taken from a 4pt cyclic bend test study on leadless chip resistor (LCR-2512) assemblies. First, the two fatigue modeling approaches are summarized for completeness: one based on the total fatigue life using the average strain state in the cross-section, and the other based on the incremental damage accumulation (propagation) rate using the local strain state at the tip of the evolving damaged zone. The corresponding model constants were termed AFC (average fatigue constants) and IFC (incremental fatigue constant).

Two different fatigue formulations were proposed, to address the effect of the non-zero cyclic mean stress, generated in these zero-to-max (R = 0) tests. The first formulation was based on an assumption of bounded fatigue strength in hydrostatic compression (BCS) and the other was based on unbounded fatigue strength under hydrostatic compression (UCS). Fatigue predictions under tensile mean stress are not significantly different between these two approaches. The 4pt cyclic bend experiment is then described briefly. A finite element model of the LCR assembly was constructed using the same global/local strategy used for the LGA assembly, to minimize computational complexity. The cyclic strain history and distribution at the failure site in the Cu trace beneath the LCR-2512 resistors were estimated and this

data was used to predict fatigue life using the two fatigue models. Results were then compared with measured fatigue life.

Only the bounded compressive model (BCS) is presented here for comparison. The BCS AFC model predicted moderate agreement with the measured cycles to failure, with regression correlation coefficient R^2 = 78%. More detailed successive initiation simulations and fatigue prediction using the IFC model provided very good agreement with the data, with R^2 = 98%! The significance of this agreement must be placed in the context of the small sample size and uncertainty about the actual failure mode. The ratio of time taken to initiate fatigue damage, to the time taken to propagate the damage to final failure, was examined for different load levels.

4.1 Introduction

With the consumer electronics industry constantly seeking out new ways to decrease the size of its products, many methods of miniaturization of electronic circuits are being explored [1-5]. With new methods, architectures, and structures come new reliability concerns. While reliability and failure studies generally focus on the solder joints of electronics, an increase in other failure sites is being noticed. This study focuses on the occurrence of copper (Cu) trace cracks just outside the solder joint, and offers up a new formation of fatigue model with model constants for the assessment of the Cu.

The experimental work in this chapter was done *a priori* by a colleague. Cu trace failures were assumed due to the lack of failures found anywhere else. Some failure

analysis was done for this case study, however no failures were found in the Cu traces either. It is therefore determined that the level of qualification for this case study is a *lower bound* to the region of fatigue failures that this configuration experienced. Since the Cu traces were not found to have failed, but this case study assesses their fatigue failure time, the results should be understood to be a life time that the traces will *at least* survive.

4.1.1 Problem Statement

In the previous chapters, the fatigue model and its constants have been developed based on the experimental work of a 3PT bend test loading profile and the accompanying FE and RS analyses. To test the efficacy of this model, this chapter demonstrates the method on a similarly structured 4PT bend test situation.

4.1.2 Background & Motivation

When assessing the mechanical durability of electronic assemblies, the dominant failure site is generally believed to be in the solder interconnect [13]. However, in many package styles, such as BGAs (ball grid arrays), LGAs (land grid arrays), MLFs (micro lead frame) and QFNs (quad flat no-lead), the Cu trace emanating from the solder pad may be the weakest failure site, especially if the solder joint is copper-defined rather than mask-defined, and if there is a sudden neck with sharp re-entrant corners where the copper trace emanates from the solder pad [12, 14, 15]. This is particularly true in situations with cyclic mechanical loading, such as cyclic quasi-static bending, vibration and repetitive drop/shock [5, 9, 10, 12-14].

3D multitechnology, multi-functional, multichip packaging technology, usually referred to as a “SiP” (system-in-package), has emerged as one of the leading methods of miniaturization. These packages can be found anywhere miniaturization is needed, from portable electronics, to smart biomechanical implants, Micro-Opto-Electromechanical Systems (MOEMS), biochemical ‘lab-on-a-chip’ sensors, and even home appliance electronic controls [7, 8]. Additionally, these packages frequently forego leads and even solder balls for further miniaturization. This generally results in stiffer, more robust solder interconnects. Consequently, the mechanically weakest point in the chain becomes the traces on the PWA [9-14].

This paper investigates the cyclic stress and strain histories in the Cu traces and attempts to quantify the accumulated fatigue damage in terms of these parameters. Prior research by the authors had focused on the solder interconnects for this package style [18, 19]. In the present study the focus is on the Cu traces.

The literature reveals many examples where the Cu trace is the weakest point in the system and the dominant failure site [11, 12]. Additionally, these failures have been found to be easily preventable by revision to the trace design. Studies show that redesigned Cu traces can indeed survive repetitive mechanical loading and that the failure site shifts elsewhere [11, 13, 20, 21].

Quantitative insights are needed into the fatigue durability of copper traces so that failures can be predicted and design guidelines can be developed to prevent these

failures. The existing literature does not have a consensus of Cu properties for electronics devices [22-25].

The decision was made to use Engelmaier's E_{Cu} and n_{Cu}. Engelmaier's work using E = 82.7GPa [22, 23] has been used most, and falls in the middle of the field as far as the literature goes.

4.2 Review of Experimental Results: 4-Pt Cyclic Bend Test, Plus Failure Analysis

The following section described the 4PT cyclic bend tests performed for a different investigation. The failure data and specimens were used as a case study for the methodology in this paper.

4.2.1 Test Specimen and Test Methods

The test specimens used for the 4pt bend test were all 2512 surface mount resistors. The solder joint and Cu trace geometry lent themselves well to a comparison with the stout LGA solder joints. The solder joints in the 4pt bend test are PbSn solder, which is different form the SAC solder used in the 3pt tests. The test coupon is shown in Figure 4-1. The PWA test coupon was 14cm by 3.65cm, and 1.65mm thick.

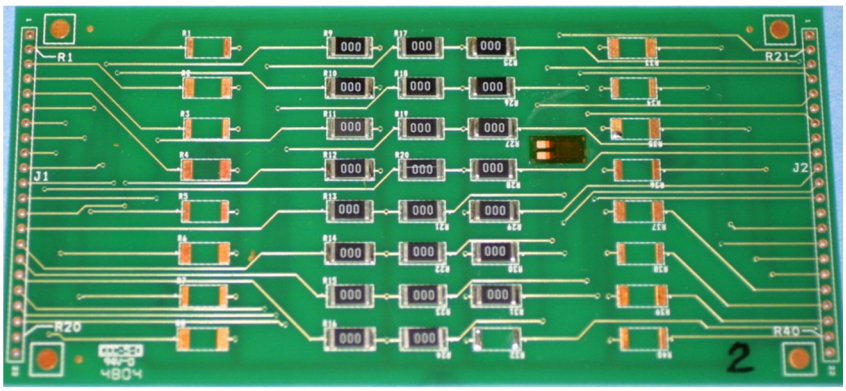

Figure 4-1: Test coupon for the 4pt bend test.

The specimens can be seen in an FE schematic in Figure 4-2. The test was a standard 4pt bend test. Two inner rollers were held stationary while two outer rollers flexed the PWA up and down.

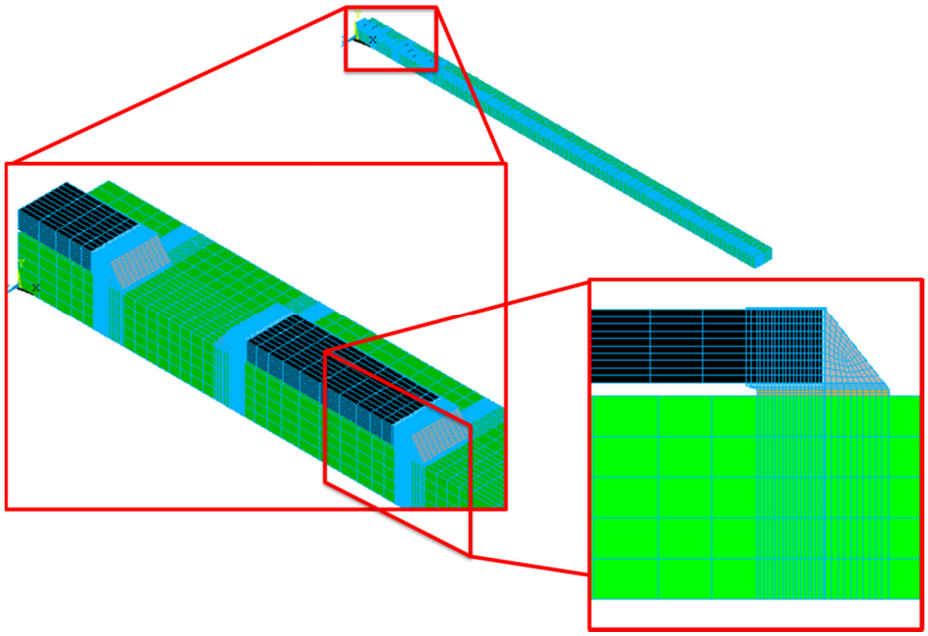

Figure 4-2: FE schematic of the 4pt bend specimens, a quarter symmetry model.

The bend test setup is shown in Figure 4-4. However, here the load will not be denoted by the "P" value in Figure 4-4. The load levels were recorded based on the gauge strain read at the max deflection. This gauge's location can be seen in Figure 4-1.

The bend test setup is shown in Figure 4-3.

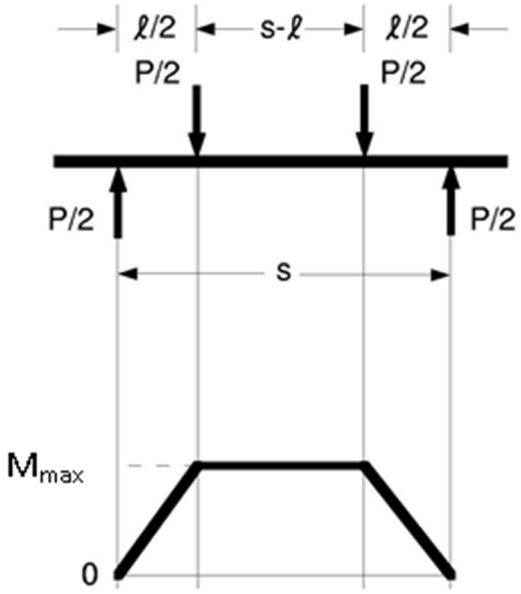

Figure 4-3: 4pt bend test setup, including bending moment diagram.

4.2.2 Fatigue Results

The individual results for the 4pt bend test can be found in Table 4-1. A plot of cycles to failure by failure set number is shown in Figure 4-4. It can be seen that a few large jumps appear in the failure data. Also note that this load level is denoted by microstrain registered on the strain gauge on the PWA during the test.

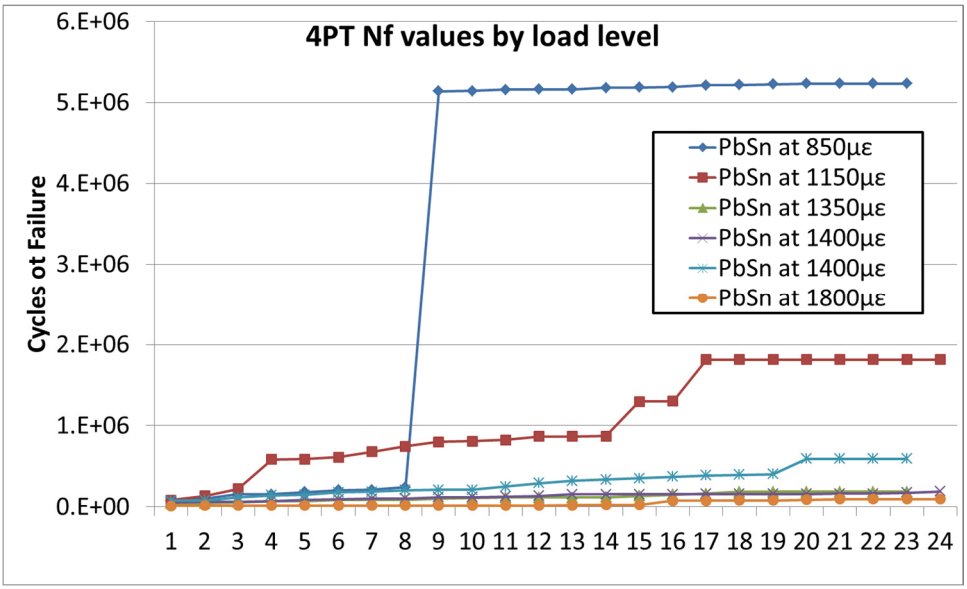

Figure 4-4: Plot of the 4pt failure data by load level. A few of the sets have large jumps in cycles to failure.

Table 4-1: Table of the failure results for the 4pt bend test. The red numbers were still functioning at that measurement.

F- Failed
S- Still Funtioning (total cycles to that point)

Coupon 2	PbSn at 850με	Coupon 9	PbSn at 1150με	Coupon 11	PbSn at 1350με	Coupon 6	PbSn at 1400με	Coupon 12	PbSn at 1400με	Coupon 13	PbSn at 1800με
F	74169.92726	F	81742	F	39243	F	56796.9	F	75427	F	13842.4
F	99808.59938	F	136645	F	43289	F	65029.52	F	79337	F	14515.06341
F	153732.3938	F	221818	F	57482	F	65614.67	F	119916	F	15521.80488
F	154933.7813	F	582762	F	66300	F	72202.1	F	140933	F	15655.8439
F	183191.1326	F	588809	F	71752	F	86590.12	F	147142	F	16485.40488
F	206703.1162	F	610821	F	84104	F	90522.4	F	179838	F	16788.89756
F	208075.6153	F	679100	F	84735	F	99096.28	F	184935	F	16817.22927
F	240398.8552	F	744624	F	88296	F	104391.17	F	207423	F	16823.29268
F	5138822.156	F	802410	F	100834	F	120618.35	F	208558	F	16865.2
F	5142635.929	F	808068	F	106938	F	120653	F	210414	F	16977.02439
F	5159456.438	F	825933	F	113460	F	126539.98	F	250819	F	17117.87805
F	5163062.756	F	866586	F	114872	F	134077.26	F	290902	F	17683.65366
F	5163178.088	F	867658	F	116695	F	153139.44	F	320389	F	19110.64878
F	5181751.817	F	872103	F	117805	F	153141.65	F	335185	F	23790.26341
F	5186547.427	F	1298599	F	134338	F	153314	F	350711	F	24731.80976
F	5191038.911	F	1299044	F	149140	F	153471.75	F	372313	F	75953.98049
F	5212053.094	S	1814253	F	163626	F	159592.96	F	385991	F	77338.8
F	5216178.956	S	1814253	F	186098	F	159592.96	F	396222	F	77885.9561
F	5224393.369	S	1814253	F	186116	F	159592.97	F	400974	F	80505.8878
S	5234651.813	S	1814253	F	186523	F	159623.11	S	591160	F	86753.83415
S	5234651.813	S	1814253	S	187841	F	162928.62	S	591160	S	94817.58537
S	5234651.813	S	1814253	S	187841	F	163223.69	S	591160	S	94817.58537
S	5234651.813	S	1814253	S	187841	F	174230.8	S	591160	S	94817.58537
		S	1814253			F	190426.3			S	94817.58537

4.3 Review of Prior Work

The previous chapter included the Finite Element model strategy leading to the developmental process of the average cross sectional fatigue constants and their fatigue model. The process is summarized here for the reader's convenience.

4.3.1 AFC Development Summary

Recall from the previous chapter that the AFCs were developed using, at once, the full cross section of the Cu trace. The von Mises equivalent total strain range and the cyclic mean stress for the second simulated bend cycle are fed in to a MATLAB solver. The MATLAB solver fits the best set of constants to the fatigue relationship using the experimental cycles-to-failure as the "N_f".

A generalized strain-life power-law model, corrected for the average hydrostatic stress at the failure site, is used to describe the fatigue durability of the Cu material if one is using an unbounded compressive strength (UCS) or bounded compressive strength (BCS) model. For this study, the relative advantages of UCS or BCS are not addressed, however both options are presented. In the case of the UCS model, the standard modified Morrow fatigue model is used for the compressive cyclic mean stress.

The model constants are determined iteratively, along with the mechanical elastic-plastic constitutive properties, starting with the initial model constants available from earlier in-house studies of PTH fatigue. The model constants were estimated by fitting this model to the measured cycles-to-failure of the experiments, using a least-square regression scheme. Since some of the model constants in the fatigue model are related to those in the stress-strain model constants, iteration was needed to match the S-N model constants to the stress-strain curve.

4.3.2 IFC Development Summary

Much like the process of development of the AFCs, this process began with finite element simulation. In fact, the FE simulations for the AFC process are each the first of 10 successive models that needed to be run for each trace and loading configuration permutation. These are examples of "damage zone length zero" (DL0) models.

The Cu trace cross sections, in the FE model, had 30 elements in an arrangement of three elements across the height of the trace and 10 elements across the width of the trace. Each of those ten sets of 3 were considered a discrete length of the damage zone. A set of simulations were run for each trace configuration and load level that had a different number of damage zones removed, simulating that they had already failed. Each of the 240 simulations were post processed to mine the von Mises equivalent strain range and cyclic mean stress experienced by each element at the cross section, if it still existed. The three elemental values for each column were averaged together to give one value per cross sectional column.

The stress and strain data needed for the MATLAB code to solve for the damage and eventually life were mined. The strains are then used to calculate discrete N_fs. These Discrete N_fs are then compiled in to a cumulative set of damage per cycle. Finally, the Total N_fs are calculated.

A MATLAB code is then used to find the best set of fatigue constants that best minimize the error between the Total N_fs calculated by the UCS or BCS model, and the N_fs observed from experiment.

4.4 Modeling and Simulation of 4-Pt Cyclic Bend Test

The global model of the 4pt bend test can be seen above in Figure 4-2. Again the global/local modeling strategy was used. The local model can be seen in Figure 4-5. This figure also shows that the local model is a symmetric model, just like the global model, since the trace is at the far edge. This means that the actual trace width is twice the model's trace width. This also means that this model must assume "2-sided propagation", meaning the crack will be assumed to be growing from both sides at the same time. This assumption is reasonable since in the model of the 3pt bend specimen the strain fields were found to be almost the same at each end of the trace. The crack could then be expected to start at either end. This model assumes it started at both.

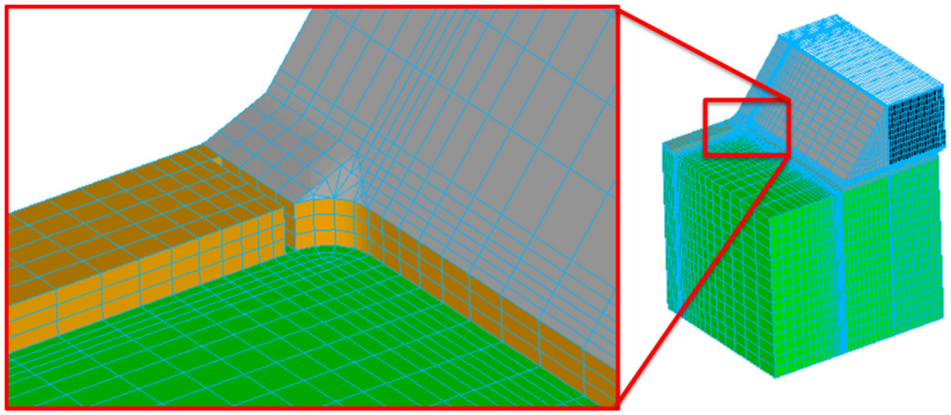

Figure 4-5: Local model with detailed inset. This model is half symmetric, as opposed to the 3pt model. This trace is also the DL8 model (half symmetry).

4.4.1 FEA Cyclic Results

Similarly to the 3pt bend tests, for the 4pt tests, the average cross sectional values are collected per load level and trace configuration. For this case study we are only presenting trace B, the middle solder joint. Trace B is the middle trace of the global model, the exaggerated deformed shape of which can be seen in Figure 4-6a. Figure 4-6b is showing the contour levels of the total equivalent strain. Again, this global model provides the boundary conditions for the local models for the AFC and IFC methods. The deformed local model's copper with accompanying total equivalent strain contours can be seen in Figure 4-7

.

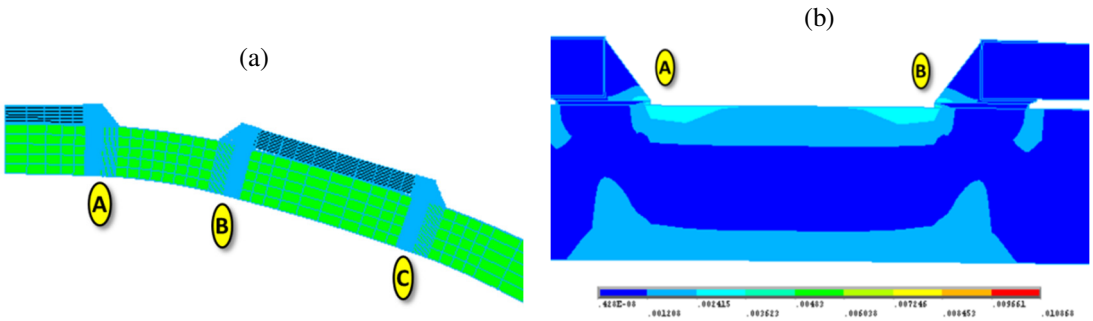

Figure 4-6: Exaggerated deformation and equivalent strain contours of the 4PT bend global FE model. The trace designation letters are shown in yellow ovals.

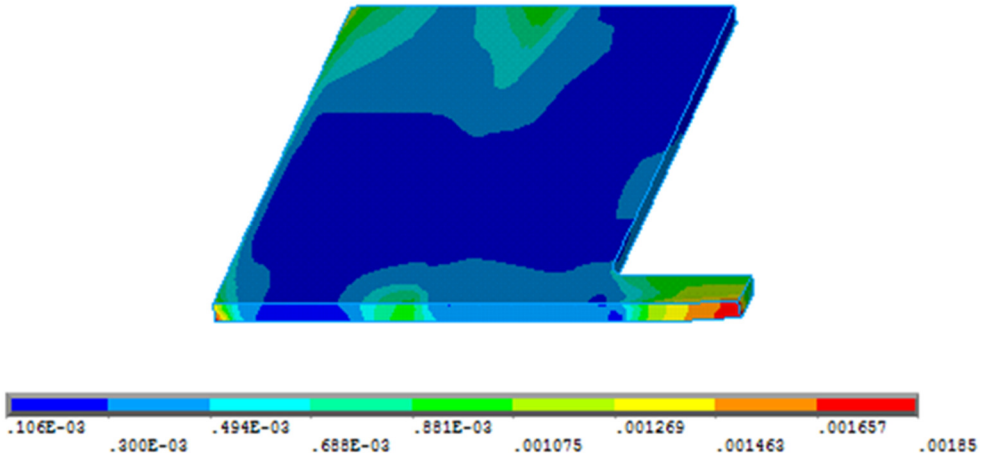

Figure 4-7: Deformed local model's Cu layer and equivalent strain contours.

A table showing example AFC output is shown in Table 4-2. Similarly, a matrix of values for the IFC model are collected, and an example of the total strain range values are shown in Table 4-3.

Table 4-2: Table of AFC model elastic strain ranges for all loads.
The negative sign denotes the bottom of the range. Positive is the top.
"EPEL" denotes elastic strain, "EPPL" is plastic strain, and "HPRES" is hydrostatic pressure.

	EPEL B	EPPL B	HPRES B
-850	8.31E-05	-1.5E-06	3.018
850	-0.0003	-1.7E-06	-10.425
-1150	9.46E-05	-4.1E-06	3.295
1150	-0.00037	-4.7E-06	-12.85
-1350	0.000103	-8.2E-06	3.25
1350	-0.00042	-9.2E-06	-14.574
-1400	0.000105	-9.4E-06	3.232
1400	-0.00043	-1.1E-05	-15
-1800	0.000134	-2.3E-05	2.985
1800	-0.0005	-2.7E-05	-18.285

Table 4-3: Sample IFC total strain data for the 4pt tests, trace configuration B.

EPTO	0	1	2	3	4
0	0.000723	0.000589	0.000535	0.000514	0.000506
1		0.000942	0.000458	0.000523	0.000501
2			0.00097	0.000473	0.000483
3				0.00101	0.000528
4					0.001131

4.4.2 AFC Model Results

The AFC model predicted N_f results which correlated with the experimental results with an R^2 value of 78%. The mean family plot can be seen in Figure 4-8. A plot of the N_f correlation can be seen in Figure 4-9.

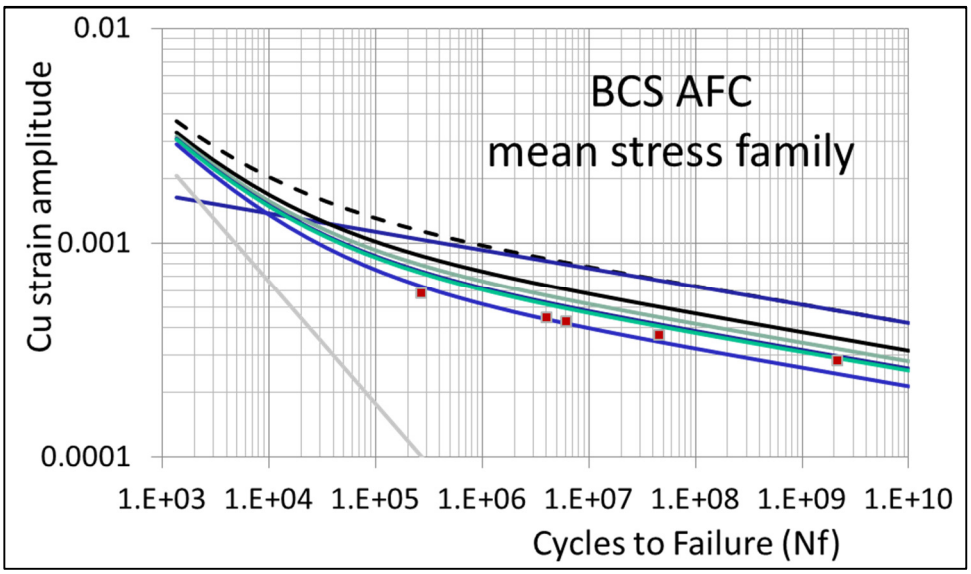

Figure 4-8: Mean stress family based on the BCS AFC model. it can be seen that the data are further in to the HCF range than the 3pt.

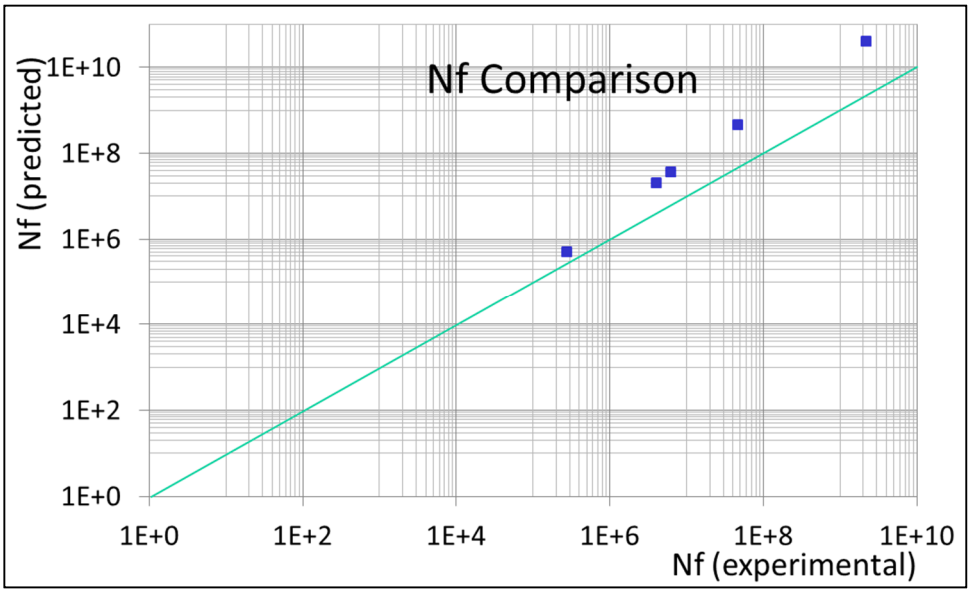

Figure 4-9: Nf comparison between the model predicted values and the experimentally observed values.

4.4.3 IFC Model Results

The stress and strain data needed for the MATLAB code to solve for the damage and eventually life were mined into charts like the example in Table 4-3. The strains are then used to calculate discrete N_fs, as seen in Table 4-4, for each cell of Table 4-3. These Discrete N_fs are then compiled in to cumulative asset of Damage per Cycle, Table 4-6. Cumulative N_fs, Table 4-5, are calculated using each cell's previous row's values of Total Damage and current values of Damage per Cycle, while the Total Damage (Table 4-7) cells are solved using that row's leading edge Cumulative N_f and the current Damage per cycle. Finally, the Total N_fs (Table 4-8) are calculated using the previous row's Total N_f and the current row's leading edge Cumulative N_f.

Table 4-4: Example table showing the discrete Nfs calculated from the above Table 4-3

		column				
		1	2	3	4	5
Cumulative Nfs	0	1870400	43577000	178240000	328240000	426660000
	1		82710	173806779	140425233	307137636
	2			59681	64145367	58331378
	3				43958	26731559
	4					27293

Table 4-5: Example table showing the Cumulative Nfs calculated for B_1400

		column				
		1	2	3	4	5
Cumulative Nfs	0	1870400	43577000	178240000	328240000	426660000
	1		82710	173806779	140425233	307137636
	2			59681	64145367	58331378
	3				43958	26731559
	4					27293

Table 4-6: Damage per Cycle calculated for B_1400

Damages per Cycle	column 1	2	3	4	5
0	5.346E-07	2.295E-08	5.610E-09	3.047E-09	2.344E-09
1		1.157E-05	5.693E-09	7.081E-09	3.242E-09
2			1.657E-05	1.549E-08	1.706E-08
3				2.259E-05	3.720E-08
4					3.637E-05

Table 4-7: Total Damage calculated for B_1400

Total Damage	column 1	2	3	4	5
0	1	0.042921725	0.010493716	0.00569827	0.004383818
1		1	0.010964594	0.006283908	0.00465193
2			1	0.00720847	0.005670314
3				1	0.007305407
4					1

Table 4-8: Total Nfs for each discrete damaged segment to fail.

Total Cycles	column 1	2	3	4	5
0	1870400	1870400	1870400	1870400	1870400
1		1953110	1953110	1953110	1953110
2			2012791	2012791	2012791
3				2056749	2056749
4					2084042

The benefits can be seen in Figure 4-13. Here, the two horizontal lines are the *Nf* predicted using the RS from the AFCs (top line) and the *SNf* (scaled *Nf*) which is just a linear scaling of the *Nf* value by the initiation to propagation ratio (IPR). The curved line is the line plotted by the values in Table 4-3 against the distance across the trace width. The curve of this line is ever so slight. The IFC model predicted that the IPR for these data is 90%, so a peak is barely noticeable.

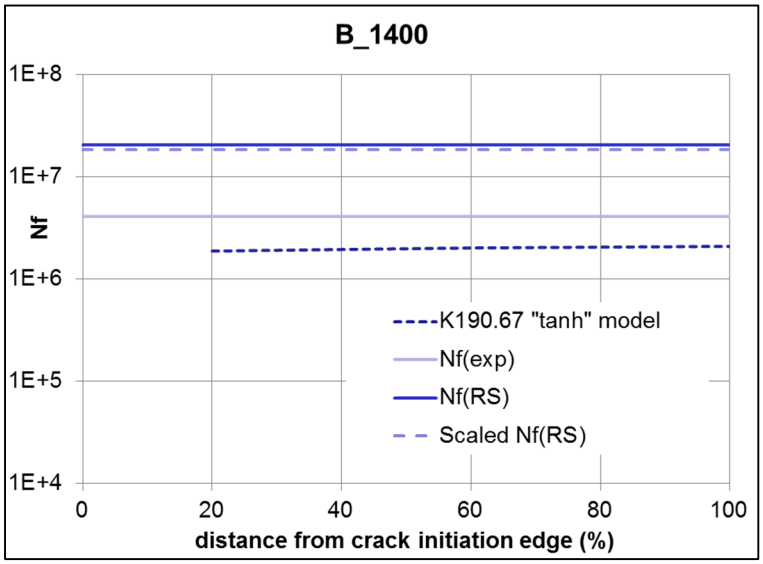

Figure 4-13: Plot of TNfs across the trace width for a K value of 190.67MPa using the tanh model.

The IFC model predicted N_f results which correlated with the experimental results with an r-squared value of 98%. The mean family plot can be seen in Figure 4-10. A plot of the Nf correlation can be seen in Figure 4-11.

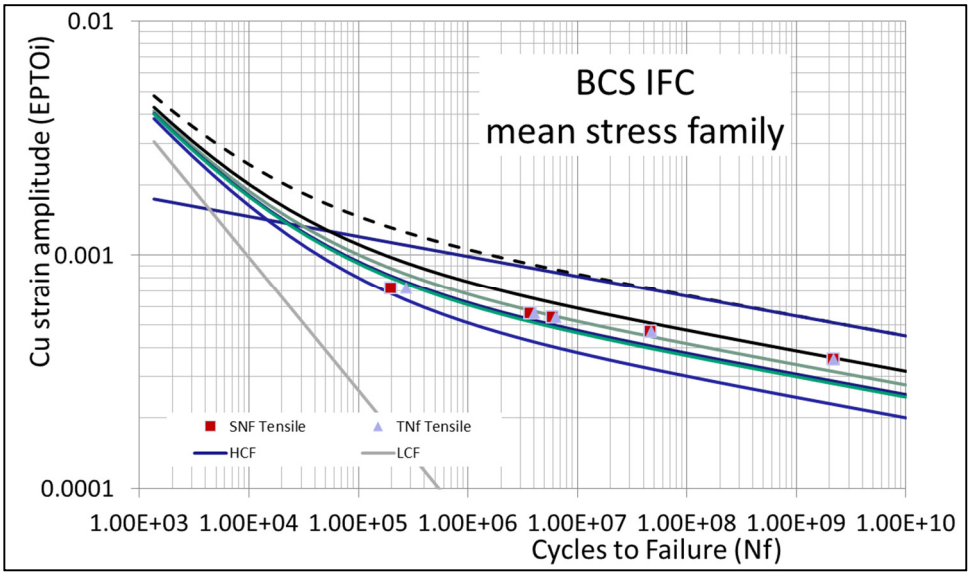

Figure 4-10: Mean stress family based on the BCS IFC model, showing both cycles to initiation and cycles to failure.

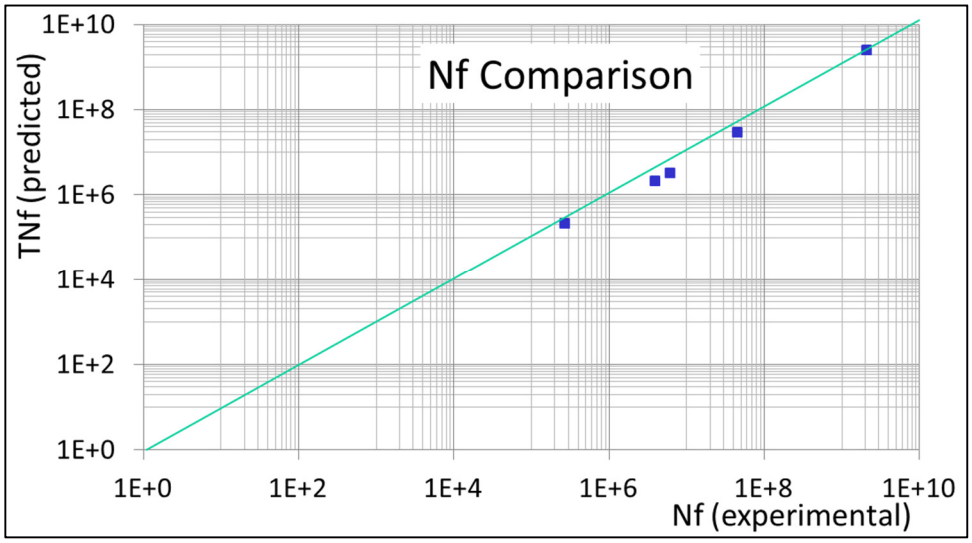

Figure 4-11: Nf comparison between the model predicted values and the experimentally observed cycles to failure.

Again, the two interesting relationships: IPR vs a certain strain ratio and IPR vs a certain stress ratio are shown in Figure 4-16 and Figure 4-17. The values of the ratio are much higher in this 4pt test than were in the 3pt test.

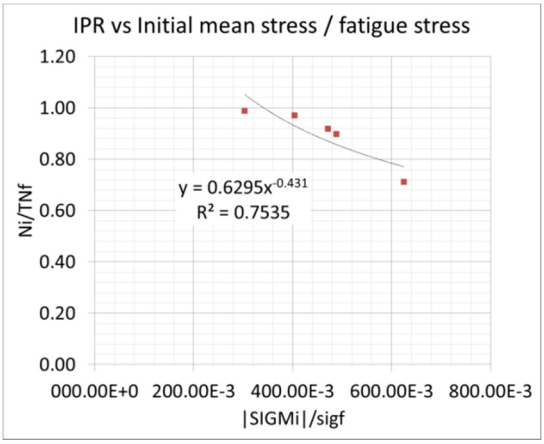

Figure 4-16: IPR compared to the ratio of the mean stress in the first damaged zone segment to the fatigue strength.

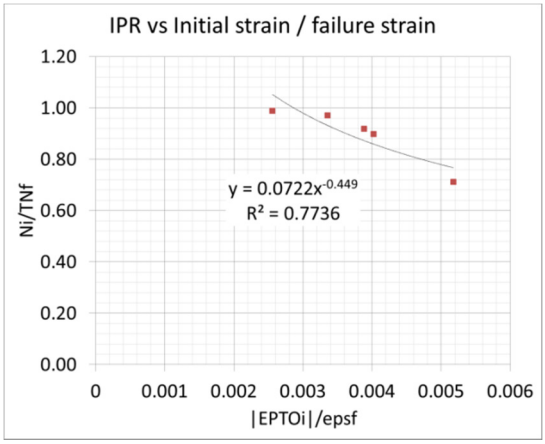

Figure 4-17: IPR compared to the ratio of the strain range in the first damaged zone segment to the fatigue ductility.

4.5 Summary & Discussions

The fatigue models and methods developed in Chapters 2 and 3 for copper traces in LGA assemblies, were verified for another independent data set taken from cyclic 4pt

bend testing of LCR assemblies. The 4pt bend test specimen was subjected to the same computational analysis and process of fatigue life prediction, using the constants and material models already established in the previous chapters: the AFC method used a fatigue strength of 134.66MPa with a corresponding fatigue ductility of 10%, which comes from the Ramberg-Osgood model when the monotonic K value is 190.67MPa. The IFC method used a fatigue strength of 141.66MPa with a corresponding fatigue ductility of 14%.

The total fatigue life model with AFC properties provided moderate correlation to the measured fatigue life with R^2 =78%. The incremental damage accumulation model with IFC properties provided much stronger correlation with the measured fatigue life with R^2 = 98%. However the sample size used in this case study was very small.

The AFC and IFC fatigue methods performed reasonably well for the 4pt bend test case study, thus providing confidence in the proposed modeling approaches, proposed fatigue models and proposed model constants. The IFC predicted a much closer result to the experimental cycles to failure, and this was expected since it is a more detailed modeling strategy.

Chapter 5: Summary

A brief summary of the fatigue methodology follows. First presented is a summary of the dissertation outcomes and the motivation behind the research. Also included are conclusions that can be drawn from the work, and discussion of the implications of the outcomes.

In the next section the impact of this work is outlined in bullet form. This paper offers a number of contributions to the field of electronics reliability in general, and the fatigue modelling of Cu, specifically.

The last section presents the limitations of the scope of this work. Along with these limitations, future work is presented as ways to improve upon or expand the purview of this study.

5.1 Conclusions & Discussions

This dissertation investigates the fatigue life of copper (Cu) traces on printed wiring assemblies (PWAs) under quasi-static cyclic mechanical bending, using experimental results from a set of 3pt cyclic bend tests, and detailed modeling using 3D elastic-plastic finite element analysis (FEA) and response surfaces (RS). This is a very important class of problems in the microelectronics literature because the burgeoning miniaturization aspect of microelectronics is creating newer and updated package architectures. These architectures sometimes push the failure sites to different locations in the assembly, such as the Cu trace just outside the footprint. This increase in occurrences demands an increase in attention and study. As discussed in Chapter 1, many researchers have reported this failure mode, but this

problem has not received sufficient attention in the literature thus far from the point of view of fatigue model development.

3pt cyclic bend tests were conducted on land grid array (LGA) assemblies during this investigation, with the initial expectation of encountering fatigue failures in the SAC305 solder joints. However, after much failure analysis, the failure site was found to be in the Cu traces just outside the footprint of the solder joint. A FE model (using a hierarchical global-local modeling strategy) was used to simulate the flexure and determine the stress and strain histories occurring at the failure site during repeated cyclic loading and unloading. Due to process-related uncertainties in the copper material properties, parametric studies were conducted for a range of material properties (elastic-plastic stress-strain curves for the copper), geometries and load amplitudes, and the outcome was captured in a polynomial response surface model.

The failure data from the experiments was collected and used in conjunction with this response surface model, to develop a modified version of the generalized Coffin-Manson fatigue model and model constants that best fit the behavior observed.

Since the loading zero-to-max (R=0), a mean stress correction factor was needed. It was discovered that the standard mean stress correction factors from the literature (e.g. modified Morrow model or Sines model) would not suffice, and this investigation developed a new model based on a “tanh” term which forced a saturation of the mean stress effect at higher levels. This “tanh” term was also considered for compressive loading, termed the BCS model (“B” for “bounded”), but

the standard unbounded model (Sines model) is presented alongside it, termed the UCS model. A detailed iterative process was developed to simultaneously adjust the Cu constitutive model constants as well as the compatible set of fatigue constants needed to satisfy the observed behavior. This model was based on the average cross section of the entire trace, and its fatigue constants were termed average fatigue constants (AFCs). The advantage of this model is its comparative simplicity. It is a slight modification to the modified Morrow fatigue model, and its implementation is only a slight departure from existing methods. Some in industry prefer the full-cross-section-at-once treatment of fatigue assessment. And of course, if failure analysis of the test specimens show that the failure site is more of a direct, single step crack failure, the AFC approach is more appropriate. However, as in this study, sometimes the failure site is more of a path of successively growing damage instead of a mathematically clean crack. For this aspect, this study developed the next approach.

To further the study to accommodate the successively growing damage path that can occur instead of the clean mathematical crack, a successive initiation method was used to estimate what fraction of the measured fatigue life was spent in initiating the fatigue damage and what fraction was spent in propagating it to failure. The constitutive model used in this part of the study is the same as was obtained from the AFC constants, using the iterative scheme discussed earlier. The process used here is based on a concept of successive failures of the leading edge finite elements ahead of the damage path, thus creating incremental damage initiation. The corresponding fatigue constants are termed the incremental fatigue constants (IFCs).

This method allows separate estimates of the initiation life and propagation life. More importantly, this provides a revised set of modified Coffin-Manson fatigue constants that are far more generic and can be used to assess fatigue damage initiation in similar copper material in structures of any geometry, based on the local load conditions at the failure site. Thus the IFCs can be used for copper traces of any geometry, unlike the AFCs.

Finally, a case study was presented on a 4pt cyclic bend test where the methodology is applied to a quasi-static cyclic mechanical bend test of slightly different solder/trace configuration. The test specimen here consists of leadless chip resistor (LCR-2512) assemblies. The Cu trace fatigue model performed well in this case study of a 4pt bend test. As expected, the IFC predictions provided better agreement with the test data than was possible with the AFC predictions. This further confirms the fact that the IFC constants and method should be more generic for extension to other trace geometries (than the one used to derive the model constants). However there was limited number of specimens in this data set and more case studies should be performed to investigate deeper in to the viability and applicability of the method, and the statistical confidence in the prediction values.

5.2 Dissertation Contributions

The contributions of this thesis include:

- New methodology for mean stress correction in the generalized Coffin-Manson fatigue model.

- A detailed iterative methodology to determine both material constitutive model and fatigue properties simultaneously from fatigue test data.

- New fatigue model constants for predicting fatigue damage initiation and propagation for copper trace failures in microelectronic assemblies under quasi-static flexural loading.

- Insights into the relative magnitudes of fatigue damage initiation life vs fatigue damage propagation life, of PWA copper traces under typical cyclic flexural loads.

- A method for qualifying successive damage propagation under quasi-static cyclic bending of polycrystalline metals, which is more appropriate to the geometry and physics of this damage mode than fracture mechanics.

- Detailed global-local, 3D, elastic-plastic finite element modeling strategy for copper traces in microelectronic assemblies, validated with test results.

- A method for transforming a vast number of computationally intensive nonlinear finite element models into a small set of response surface calculations that cut computation time down by large amounts.

5.3 Limitations and Future Work

- The constants that were held and those that were varied could be changed up. For example, the hardening exponent, n, was held constant as per Engelmaier's work. But a more comprehensive AFC method could be

developed wherein n is included in the Response Surface and varied to find the best fit. This in turn will vary b and c as well.

- Model is limited in strain rate to quasi-static cyclic bending. Future work could include investigating expanding the method out to higher strain rates like vibration, shock, impact and drop.

- Model is limited in details about the effect of solder type on the results. Parametrics for different solder alloys, different surface finishes, different substrates, and different copper qualities could be performed.

- The case study validation is limited in terms of statistically significant sample sets. Further validation for other geometries (other component types and trace geometries) and loading conditions such as PWA warpage of different deformation mode shapes.

- It is possible that many of the failures in the compressive failure data and the case study failure data were not Cu trace failures. More comprehensive failure analysis could be done to determine the specific failure modes and sites. Then, better data sets can be developed, segregated by failure modes.

- The range of compressive mean stress in the test data was very limited. If the range is expanded in the test data, the relationship of compressive mean stress and lifetime benefit can be better investigated. The debate between UCS and BCS can then better be served.

Acknowledgments

This work is sponsored by the members of the CALCE Electronic Products and Systems Consortium at the University of Maryland, College Park.

References

[1] H. M. B. Bird, “Approaches to electronic miniaturization,” *IEEE Transactions on* Components*, Packaging, and Manufacturing Technology, Part A,* vol. 18, no. 2, pp. 274-278, 1995.

[2] J. Adam, and M. Bird, “SiP Technology Offers Packaging Alternatives for Design,” *Advanced Packaging,* vol. 13, pp. 16-20, 2004.

[3] A. Elshabini, G. Wang, and F. Barlow, “Future trends in electronic packaging,” in Smart Structures and Materials 2006: Smart Electronics, MEMS, BioMEMS, and Nanotechnology San Diego, CA, USA, 2006.

[4] F. Murray, “Silicon Based System-in-Package: passive integration technology combined with advanced packaging and system based design tools to allow breakthrough in miniaturization,” in Proceedings of the Bipolar/BiCMOS Circuits and Technology Meeting, Santa Barbara, California, USA, 2005, pp. 169 - 173.

[5] D. Farley, Y. Zhou, A. Dasgupta *et al.*, “Reliability of RF SiP Assemblies under mechanical loads,” in 1st International Congress on Microreliability and Nanoreliability in Key Technology Applications, Berlin, Germany, 2007.

[6] A. Dasgupta, M. Pecht, and B. Mathieu, “Design-of-experiment methods for computational parametric studies in electronic packaging,” *Finite Elements in Analysis and Design,* vol. 30, no. 1-2, pp. 125-146, 1998.

[7] D. Farley, A. Dasgupta, and J. Caers, “Mechanics of Adhesively Bonded Flip-Chip-on-Flex Assemblies. Part II: Effect of Bump Coplanarity on Manufacturability and Durability of Non-Conducting Adhesive Assemblies,” *Journal of Adhesion Science and Technology,* vol. 22, no. 14, pp. 1757-1780, 2008.

[8] D. Farley, A. Dasgupta, and J. F. J. M. Caers, “Characterizing Non-Conductive Adhesives using Finite Element Analysis: Residual Stress Determination,” in Society of Experimental Mechanics Annual Conference & Exposition, Portland, OR, USA, 2005.

[9] D. Y. R. Chong, F. X. Che, J. H. L. Pang *et al.*, “Drop impact reliability testing for lead-free and lead-based soldered IC packages,” *Microelectronics and Reliability,* vol. 46, no. 7, pp. 1160-1171, July, 2006.

[10] D. Y. R. Chong, K. Ng, J. Y. N. Tan *et al.*, “Drop test reliability assessment of leaded & lead-free solder joints for IC packages,” in EPTC 2004. Proceedings of 6th Electronics Packaging Technology Conference, Singapore, 2004, pp. 210-217.

[11] Z. Jing, L. Hai, and J. Lee, “Board Level Cyclic Bending Test for MCP Package,” in EPTC 2007. 9th Electronics Packaging Technology Conference, Singapore, 2007.

[12] K. E. Ong, W. K. Loh, C. W. Wong *et al.*, “Industry Drop Tests in Solder Joint Reliability Study of Molded Flip Chip Package,” in EMAP 2006. International Conference on Electronic Materials and Packaging, Hong Kong, 2006, pp. 1-7.

[13] A. Syed, T. Y. Tee, H. S. Ng *et al.*, “Advanced analysis on board trace reliability of WLCSP under drop impact,” *Microelectronics Reliability,* vol. 50, no. 7, pp. 928-936, 2010.

[14] Y. Yuan, and B. J. Carpenter, “Trace crack in molded thin substrate package, root causes and FEM modeling,” in ICEPT 2003. Fifth International Conference on Electronic Packaging Technology Proceedings, Shanghai, China, 2003, pp. 449-454.

[15] A. Kujala, T. Reinikainen, and W. Ren, “Transition to Pb-free manufacturing using land grid array packaging technology,” in ECTC : electronic components

& technology conference, San Diego CA, 2002, pp. 359-364.

[16] J. Varghese, and A. Dasgupta, “An experimental approach to characterize rate-dependent failure envelopes and failure site transitions in surface mount assemblies,” *Microelectronics Reliability,* vol. 47, no. 7, pp. 1095-1102, 2007.

[17] C. Zhan, H. Chang, T. Chang *et al.*, “Experimental/numerical analysis of halogen-free printed circuit board assembly under board level drop test,” in International Microsystems, Packaging, Assembly, and Circuits Technology Conference, Taipei, 2009, pp. 381-384.

[18] D. Farley, A. Dasgupta, and J. F. J. Caers, “Qualification Of A System-in-Package (SiP): A Physics-of-Failure (PoF) Perspective,” in Proceedings of the ASME International Mechanical Engineering Congress and Exposition, ASME IMECE, Chicago, Illinois, USA, 2006.

[19] D. Farley, Y. Zhou, A. Dasgupta *et al.*, “Qualification of SiP Products: Quasi-Static Cyclic Mechanical Bending,” in Proceedings of the ASME International Mechanical Engineering Congress and Exposition, ASME IMECE, Seattle, Washington, USA, 2007.

[20] D. Farley, Y. Zhou, F. Askari *et al.*, “Copper trace fatigue models for mechanical cycling, vibration and shock/drop of high-density PWAs,” *Microelectronics Reliability,* vol. 50, no. 7, pp. 937-947, July, 2010.

[21] T. Y. Tee, H. S. Ng, A. Syed *et al.*, “Design for board trace reliability of WLCSP under drop test,” in EuroSimE 2009. Proceedings of the 10th International Conference on Thermal, Mechanical and Multi-Physics Simulation and Experiments in Micro-Electronics and Micro-Systems, Delft, NL, 2009, pp. 1-8.

[22] W. Engelmaier, “Results of the lPC Copper Foil Ductility Round-Robin Study,” 1987, pp. 66.

[23] W. Engelmaier, and A. Wagner, “Fatigue Behaviour and Ductility Determination for Rolled Annealed Copper Foil and Flex Circuits on Kapton,” *Circuit World,* vol. 14, no. 2, pp. 30-38, 1993.

[24] H. Mughrabi, and H. W. Höppela, “Cyclic deformation and fatigue properties of very fine-grained metals and alloys,” *International Journal of Fatigue,* vol. 32, no. 9, pp. 1413-1427, September 2010, 2010.

[25] Y. Takahashi, H. Hirakata, and T. Kitamura, “Quantitative evaluation of plasticity of a ductile nano-component,” *Thin Solid Films,* vol. 516, pp. 1925-1930, 2008.

[26] W. Ramberg, and W. R. Osgood, “Description of stress-strain curves by three parameters,” *NACA Technical note,* vol. 902, 1943.

[27] L. Collini, “Fatigue crack growth resistance of ECAPed ultrafine-grained copper,” *Engineering Fracture Mechanics,* vol. 77, no. 6, pp. 1001-1011, 2010.

[28] G. Khatibi, J. Horky, B. Weiss *et al.*, “High cycle fatigue behaviour of copper deformed by high pressure torsion,” *International Journal of Fatigue,* vol. 32, no. 2, pp. 269-278, 2010.

[29] S. Stanzl-Tschegg, H. Mughrabi, and B. Schoenbauer, “Life time and cyclic slip of copper in the VHCF regime,” *International Journal of Fatigue,* vol. 29, no. 9-11, pp. 2050-2059, 2007.

[30] S. Stanzl-Tschegg, and B. Schönbauer, “Mechanisms of strain localization, crack initiation and fracture of polycrystalline copper in the VHCF regime,” *International Journal of Fatigue,* vol. 32, no. 6, pp. 886-893, 2010.

[31] D. Tromans, and R. Sun, “Intergranular/transgranular fatigue of copper: influence of environment on crack path and propagation rates,” *Materials Science and Engineering A,* vol. 219, no. 1-2, pp. 56-65, 1996.

[32] A. Vinogradov, M. Maruyama, and S. Hashimoto, “On the role of dislocation hardening in the monotonic and cyclic strength of severely plastically deformed metals,” *Scripta materialia,* vol. 61, no. 8, pp. 817-820, 2009.

[33] B. Jian-qiang, S. Kang-ning, F. Run-hua *et al.*, “Preparation of Bulk Ultrafine-grained 2A12 Alloy Material Pressed by ECAP,” *Journal of Synthetic Crystals,* vol. 2, 2006.

[34] C. Lee, K. Park, and J. Lee, “Plasticity improvement of a bulk amorphous alloy based on its viscoelastic nature,” *Scripta materialia,* vol. 59, no. 8, pp. 802-805, 2008.

[35] T. Liu, W. Zhang, S. Wu *et al.*, “Mechanical properties of a two-phase alloy Mg-8% Li-1% Al processed by equal channel angular pressing,” *Materials Science and Engineering A,* vol. 360, no. 1-2, pp. 345-349, 2003.

[36] M. Shariyat, “A fatigue model developed by modification of Gough's theory, for random non-proportional loading conditions and three-dimensional stress fields,” *International Journal of Fatigue,* vol. 30, no. 7, pp. 1248-1258, 2008.

[37] T. Mattila, P. Marjamaki, L. Nguyen *et al.*, “Reliability of chip scale packages under mechanical shock loading,” in Electronic Components and Technology Conference, Reno, NV, 2006, pp. 584-589.

[38] S. Hong, and R. Weil, “Low cycle fatigue of thin copper foils,” *Thin Solid Films,* vol. 283, no. 1-2, pp. 175-181, 1996.

[39] G. Sines, "Metal Fatigue,(edited by G. Sines and JL Waisman)," McGraw Hill, NY, 1959.

[40] A. Boresi, and K. Chong, *Elasticity in engineering mechanics*: Wiley-Interscience, 2000.

[41] RSwarbrick. "Yield_surfaces.svg," 10 September, 2010; http://en.wikipedia.org/wiki/File:Yield_surfaces.svg.

[42] K. Smith, T. Topper, and P. Watson, “A stress-strain function for the fatigue of metals(Stress-strain function for metal fatigue including mean stress effect),” *Journal of Materials,* vol. 5, pp. 767-778, 1970.

[43] K. Walker, S. Pendleberry, and R. McElwee, “Effects of environment and complex load history on fatigue life,” *ASTM STP,* vol. 462, pp. 1-14, 1970.

[44] M. Alqam, R. M. Bennett, and A.-H. Zureick, “Three-parameter vs. two-parameter Weibull distribution for pultruded composite material properties,” *Composite Structures,* vol. 58, no. 4, pp. 497-503, 2002.

[45] "ANSYS® Academic Research," *Release 11.0*, ANSYS, Inc.

[46] G. Cuddalorepatta, and A. Dasgupta, “Viscoplastic behavior of hypo-eutectic Sn3. 0Ag0. 5Cu Pb-free alloy under creep loading conditions,” in EuroSimE 2008., Freiburg, Germany, 2008.

[47] M. Osterman, "CALCE Plated Through Hole Fatigue Model," *Guide for CALCE Software Users*, CALCE EPRC, University of Maryland, College Park, 2002.

[48] A. Fatemi, and P. Kurath, “Multiaxial fatigue life predictions under the influence of mean-stresses,” *Journal of Engineering Materials and Technology,* vol. 110, pp. 380, 1988.

[49] D. Socie, “Critical plane approaches for multiaxial fatigue damage assessment,” *Advances in multiaxial fatigue*, pp. 7-36, 1993.

[50] G. Sines, and G. Ohgi, “Fatigue Criteria Under Combined Stresses or Strains,” *Journal of Engineering Materials and Technology,* vol. 103, no. 2, pp. 82-90, 1981.

[51] J. H. Okura, “Effect of temperature and moisture on durability of low cost flip chip on board (FCOB) assemblies,” Department of Mechanical Engineering, University of Maryland, College Park, 2001.

[52] L. Ladani, and A. Dasgupta, “The Successive-Initiation Modeling Strategy for Modeling Damage Progression: Application to Voided Solder Interconnects,” in EuroSime 2006, 7th International Conference on Thermal, Mechanical and Multiphysics Simulation and Experiments in Micro-Electronics and Micro-Systems, 2006, pp. 1-6.